

# Behaviour of a novel functionally graded 3D re-entrant lattice reinforced high-performance concrete under static and dynamic compression

Yiwei Xuan<sup>a</sup>, Dianwei Gao<sup>b</sup>, Mingzhong Zhang<sup>a,\*</sup> 

<sup>a</sup> Department of Civil, Environmental and Geomatic Engineering, University College London, London, WC1E 6BT, United Kingdom

<sup>b</sup> School of Architecture and Civil Engineering, Shenyang University of Technology, Shenyang, 110870, China

## ARTICLE INFO

### Keywords:

High-performance concrete  
Metamaterials  
Functionally gradient design  
3D printing  
Impact  
Energy absorption

## ABSTRACT

This paper presents a systematic experimental study on the static and dynamic mechanical behaviour of high-performance concrete (HPC) reinforced with 3D re-entrant lattice, accounting for the effect of functionally gradient design. The uniform 3D re-entrant lattice (U) and the corresponding vertically positively and negatively graded lattices (FG1 and FG2) were designed and manufactured with 3D printing. The plain HPC (P-HPC) and HPC reinforced with U (U-HPC), FG1 (G1-HPC) and FG2 (G2-HPC) were fabricated accordingly. Static compressive and split Hopkinson pressure bar tests were then conducted to investigate the static and dynamic compressive behaviour of 3D re-entrant lattice reinforced HPC under various strain rates (i.e., 0, 28.1, 50.6, 72.0 and 100.6 s<sup>-1</sup>). Results indicate that the static compressive strength of HPC specimens is slightly improved owing to re-entrant lattice reinforcement, while the static dissipated energy of P-HPC is 55.7 %, 53.2 % and 57.5 % lower than that of U-HPC, G1-HPC and G2-HPC, respectively. Regarding dynamic compressive behaviour, although the dynamic strength of P-HPC is 11.3–24.6 % higher than that of lattice reinforced HPC at a strain rate of around 30 s<sup>-1</sup>, with the further increase of strain rates, the re-entrant lattice reinforced HPC presents higher strength improvement. G2-HPC has the highest dynamic compressive strength of 198.3 MPa at a strain rate of approximately 100.6 s<sup>-1</sup>, followed by G1-HPC, P-HPC and U-HPC. At low strain rates, the plain and lattice reinforced HPC exhibit the similar energy absorption. When the strain rate reaches around 100.6 s<sup>-1</sup>, U-HPC, G1-HPC and G2-HPC exhibit a 29.8 %, 36.8 % and 54.3 %, respectively higher dissipated energy than P-HPC. The gradient design of lattice reinforcement brings a more gradual and smooth dissipation of energy, thereby improving the overall energy absorption capacity. The excellent dynamic compressive behaviour of functionally graded 3D re-entrant lattice reinforced HPC offers a promising solution for protective structures subjected to high strain rates, including impact, blast, and seismic loadings.

## 1. Introduction

As one of the most extensively used construction materials, concrete has been developed into various types to meet the demands for different civil infrastructures. High-performance concrete (HPC), as an advanced material distinct from traditional concrete, has higher strength with improved elastic modulus, durability and lower permeability [1]. Similar to normal concrete, HPC also suffers from significant inherent brittleness [2]. To alleviate the intrinsic brittleness, steel or polymer fibres are usually incorporated into concrete [3]. However, the discrete and disordered distribution of these fibres could bring the unpredictable localised cracking patterns and impair the mechanical performance of cementitious composites [4,5]. To overcome such limitation, 3D lattices

with continuous and regular arrangement can be regarded as an advanced reinforcement to achieve an expected cracking process, improved strength, ductility and energy absorption capacity [6].

In recent years, with the rapid development of metamaterials, auxetic lattices characterised by negative Poisson's ratio (NPR) effects were proposed. Emerged as a novel structure, the auxetic structure shrinks transversely under compression and stretches transversely under tension, leading to superior engineering properties such as variable permeability, excellent shear stiffness, indentation resistance, and fracture toughness [7]. When subjected to impact loadings, different from conventional structures with positive Poisson's ratio, the auxetic lattices tend to converge towards the impact region and bring intense densification in impact area, resulting in enhanced energy absorption

\* Corresponding author.

E-mail address: [mingzhong.zhang@ucl.ac.uk](mailto:mingzhong.zhang@ucl.ac.uk) (M. Zhang).

<https://doi.org/10.1016/j.cemconcomp.2025.106261>

Received 1 May 2025; Received in revised form 15 July 2025; Accepted 27 July 2025

0958-9465/© 2025 The Authors. Published by Elsevier Ltd. This is an open access article under the CC BY license (<http://creativecommons.org/licenses/by/4.0/>).

capacity and impact resistance [8]. The superior mechanical properties and high porosity of auxetic structures provided a prospect of adding auxetic lattice reinforcement into HPC. Among various kinds of auxetic structures, re-entrant structures composed of thin ribs and linking hinges were most widely explored because of the excellent strength, elastic modulus and NPR effects [9–11].

Various studies have been focused on re-entrant lattice reinforced cementitious composites which exhibit superior stiffness, hardness and toughness by incorporating auxetic lattices, against non-auxetic lattice composites. In comparison with the passive confinement activated by lateral expansion of plain concrete under compression, the re-entrant lattice reinforcement can provide both active augmented confinement sourced from NPR effects and passive confinement activated by concrete [12]. The NPR effect of re-entrant lattice resulted in biaxial compression of concrete, thus enhancing the compressive performance. Meanwhile, the sliding difficulty of struts was increased greatly by the friction between lattices and concrete [13,14]. 3D re-entrant steel lattice reinforced concrete was found to have a 140 % higher compressive strength than unconfined concrete and around 41 % higher than conventional reinforced concrete with passive confinement. The ductility indices of auxetic lattice reinforced cementitious composites was in the range of 7.4–7.7, implying an excellent ductility and higher load bearing capacity after local fracture or buckle of struts [12,15]. The incorporation of 3D printed polylactic acid (PLA)-based re-entrant honeycomb reinforcement resulted in an 8.3 % and 19.5 % rise in static compressive strength of ultra-high performance concrete (UHPC) against the unconfined UHPC and equivalent octet lattice reinforced UHPC, respectively. With the increasing strain rate to around  $85\text{--}135\text{ s}^{-1}$ , the dynamic compressive strength of re-entrant honeycomb reinforced UHPC was superior to other composites including steel fibre reinforced UHPC, ascribed to the more pronounced auxeticity of lattices under impact and synergistic interaction between auxetics and filling materials [16]. It was also reported that the deformation patterns and energy absorption ability of auxetic lattice reinforced cementitious composites mainly depended on the relative stiffness and strength between the lattice and filler phase [17]. Besides, the transition from single re-entrant reinforcement to layered re-entrant reinforcement would enhance the shear resistance as well as overall stability and energy absorption capacity of cementitious composites [18]. To date, although large-scale engineering applications of auxetic lattice reinforced cementitious composites are still lacking, recent studies have developed different structural elements, including auxetic carbon fibre reinforced polymer (CFRP) confined concrete columns, auxetic tube confined concrete cylinders, and re-entrant steel reinforced concrete columns [12,19,20]. The excellent ductility and energy absorption capacity of cementitious protective structural elements reinforced with auxetic structures indicate their promising prospects in structural implementation subjected to dynamic loadings such as blast, earthquake and vehicle collisions [21–23].

Within the interaction between lattice reinforcement and filling materials, the geometry of lattice reinforcement plays a crucial role in determining the mechanical properties of lattices and composites [24, 25]. Hence, the introduction of functionally gradient design can emerge as a promising approach to improving the properties of auxetic lattice reinforced concrete. Functionally gradient was defined as a gradual variation in chemical compositions or structural design, which enables to tailor the mechanical responses of the materials [26]. Generally, the relative density in each layer can be graded by altering strut diameter, unit cell height, cell wall thickness and porosity [27–36]. Compared to uniform structures, the vertically relative graded lattice structures tended to exhibit a layer-wise collapse, each characterised by a short plateau region in mechanical responses [27]. Meanwhile, as to energy absorption capacity, most relative density vertically graded lattices exhibited a higher strain at onset of densification compared to the uniform counterpart [37–39]. The rapidly increasing plateau stress with strain and the higher onset densification strain contributed to superior energy absorption capability of graded structures. Although the

re-entrant lattice reinforced cementitious composites offered superior mechanical performance under static and dynamic loadings in aforementioned studies, the optimisation of lattice reinforcement geometry has been rarely explored. The introduction of functionally gradient design was expected to achieve more controllable deformation patterns and enhanced energy absorption capacity of re-entrant lattice reinforced concrete under static and dynamic compression. To date, a systematic study on mechanical performance of functionally graded 3D re-entrant lattice reinforced concrete is still lacking.

The main purpose of this study is to systematically investigate the static and dynamic mechanical behaviour of HPC reinforced with 3D re-entrant lattices, considering the effect of functionally gradient design. Firstly, the uniform 3D re-entrant lattice structure (U), a vertically positively graded structure (FG1), and a negatively graded structure (FG2) with the same relative density were systematically designed and manufactured with 3D printing using selective laser sintering (SLS) method. Then, the corresponding uniform lattice reinforced HPC (U-HPC), positively graded lattice reinforced HPC (G1-HPC) and negatively graded lattice reinforced HPC (G2-HPC) were fabricated accordingly. The plain HPC (P-HPC) was also prepared as the reference specimen for comparison. Afterwards, the static compressive tests on lattices and HPC composites were performed to explore the deformation pattern, NPR effect, stress-strain response and energy absorption capacity. Moreover, Split Hopkinson pressure bar (SHPB) tests were conducted to study the dynamic compressive behaviour of 3D re-entrant lattice reinforced HPC under different strain rates (i.e., 28.1, 50.6, 72.0 and  $100.6\text{ s}^{-1}$ ). Based on the obtained experimental results, the effects of functionally graded lattice reinforcement and strain rates on the dynamic compressive behaviour of HPC as well as the underlying mechanisms were thoroughly explored and discussed in detail.

## 2. Experimental program

### 2.1. High-performance concrete (HPC)

#### 2.1.1. Mix proportion

The mix proportion of HPC used in this study is given in Table 1. P. O52.5 Portland cement with density of  $3000\text{ kg/m}^3$  was used as the binder along with silica fume that has an average particle size of  $0.1\text{--}0.15\text{ }\mu\text{m}$  and a specific surface area of  $15\text{--}27\text{ m}^2/\text{g}$ . Silica sand with a maximum particle size below  $450\text{ }\mu\text{m}$  was used as fine aggregate. Polycarboxylate-based superplasticisers at around 2.1 % of the total binder by mass were added to improve the workability of HPC.

#### 2.1.2. Sample preparation

HPC was primarily produced through a mixing and curing process. During the mixing process, dry materials including cement, silica fume and silica sand were initially slowly mixed in the mixer for 3 min. Then, superplasticisers were added slowly and mixed thoroughly for 3 min, followed by gradual addition of water and high-speed mixing for another 2.5 min. Finally, the fresh mixture achieved the peak flowability. The slump test was conducted for all fresh HPC mixtures, indicating that the slump of P-HPC was  $207.3 \pm 2.2\text{ mm}$ .

After mixing process, the mixture was promptly cast into void cube moulds ( $70.7 \times 70.7 \times 70.7\text{ mm}^3$ ) and vibrated on a vibrating table. All samples were cured in the moulds for 1 d and then de-moulded, followed by continued curing in a standard curing chamber at a temperature of  $20 \pm 2\text{ }^\circ\text{C}$  and a relative humidity of 95 % until 28 d.

**Table 1**  
Mix proportion of HPC ( $\text{kg/m}^3$ ).

Cement	Silica fume	Sand	Water	Superplasticisers
788	200	1100	160	21

## 2.2. 3D re-entrant lattices

### 2.2.1. Geometry

Inspired from a previous study [16], Catia software was used to develop 3D re-entrant lattice structures. Fig. 1 illustrates the geometry of 2D and 3D unit cell for each structure. Both uniform and graded structures held same skeleton of 2D unit cell but different thicknesses for development of 3D structures (Fig. 1a). The re-entrant angle defined as the angle between the inclined and vertical struts was set as  $45^\circ$  [40]. The inclined and vertical struts of 2D skeleton had lengths of 11.2 mm and 19.3 mm, respectively. Fig. 1b–d demonstrates the detailed geometry of 3D unit cells of the uniform and graded lattices. The uniform structure (U) had the same strut thickness as 2.4 mm for all layers, while the strut thickness of each layer from top to bottom was set from 2.0 mm to 2.8 mm for the corresponding positively graded re-entrant structure (FG1), and from 2.8 mm to 2.0 mm for negatively graded re-entrant structure (FG2).

Fig. 2 presents a schematic diagram of the designed structures. All uniform and graded structures consisted of  $4 \times 4$  3D unit cells and kept the same volume fraction ( $V_f$ ) as 10.5 % of cementitious composites. U had a dimension of  $65.76 \times 65.76 \times 65.81 \text{ mm}^3$  (length  $\times$  width  $\times$  height), while the varying length (width) of FG1 and FG2 from 65.36 mm to 66.16 mm was adopted according to thickness of outer vertical struts.

### 2.2.2. PA12

As one of the most common printing materials for SLS method, PA12 with excellent tensile behaviour, hardness, abrasion resistance and thermal properties was used to print the designed re-entrant lattices in this study [41–43]. Uniaxial tensile tests on PA12 dog-bone specimens were conducted to measure the tensile properties of PA12, with tensile loading rate of 1 mm/min as per GB-T 1040.2–2022 [44]. Fig. 3b demonstrates the tensile stress-strain curves of three PA12 samples. The middle part of the specimen became slender, followed by a relatively smooth perpendicular fracture to the loading direction. The tensile stress-strain curves began with a nearly elastic growth to around 1.75 % strain and then fractured. The measured elastic modulus, tensile strength and elongation at break of PA12 were  $1.30 \pm 0.05 \text{ GPa}$ ,  $23.30 \pm 1.93 \text{ MPa}$ , and  $1.79 \pm 0.08 \%$ , respectively.

### 2.2.3. Specimen fabrication

The re-entrant lattices were printed through SLS 3D printing using an EOS p7 3D printer. To facilitate maintaining the lattice structures in the

mould to achieve a centred reinforcement accompanied with a protective layer during the casting process, twelve protrusions at 2 mm height were symmetrically positioned on the surface of neutral struts in the four directions (Fig. 4a). The 3D printed samples of U, FG1 and FG2 are shown in Fig. 4b–d.

## 2.3. 3D re-entrant lattice reinforced HPC

Three types of 3D re-entrant lattice reinforced HPC (i.e., U-HPC, G1-HPC and G2-HPC) were fabricated and investigated in this study, the casting and vibrating process of which are shown in Fig. 5. Compared to P-HPC, the re-entrant lattices were placed in the middle of the mould at first, which can be fit through the protrusions on both sides and bottom. Then, the fresh HPC was smoothly injected into the mould through the void in the lattice, followed by continuous vibration to ensure that HPC was filled into the lattice structure from bottom to top. The curing and demoulding process kept the same as that of P-HPC. To ensure reliability of the test results, three repetitions were designed for four HPC specimens for compressive tests and the average values were adopted for analysis.

## 2.4. Test methods

### 2.4.1. Static compressive test

The uniaxial quasi-static compressive test on three lattice structures with different gradient design was performed using a WDW-100 microcomputer-controlled electronic universal testing machine with loading capacity of 100 kN. The specimen was placed on the lower platen of the testing machine, with the vertical centre aligning with the centre of the lower platen, as illustrated in Fig. 6. The loading was employed along the manufacturing orientation of the lattice structures. The upper platen compressed the specimen up to 80 % displacement (around 52.6 mm). The loading rate was constantly set as 3.95 mm/min to achieve a strain rate of  $0.001 \text{ s}^{-1}$ . The displacement data was collected through linear variable differential transformers (LVDT) with accuracy of  $10^{-5} \text{ mm}$ . Meanwhile, a digital camera was placed in front of the machine to record the deformation patterns and obtain the Poisson's ratios of the specimens under static compression.

Due to the incorporation of functionally graded design, the Poisson's ratio of each layer of the 3D re-entrant lattice presented significant variations with the increase of strain. To investigate the auxetic behaviour of the lattices, the average Poisson's ratio of each layer was recorded and compared. As shown in Fig. 6, four reference points were

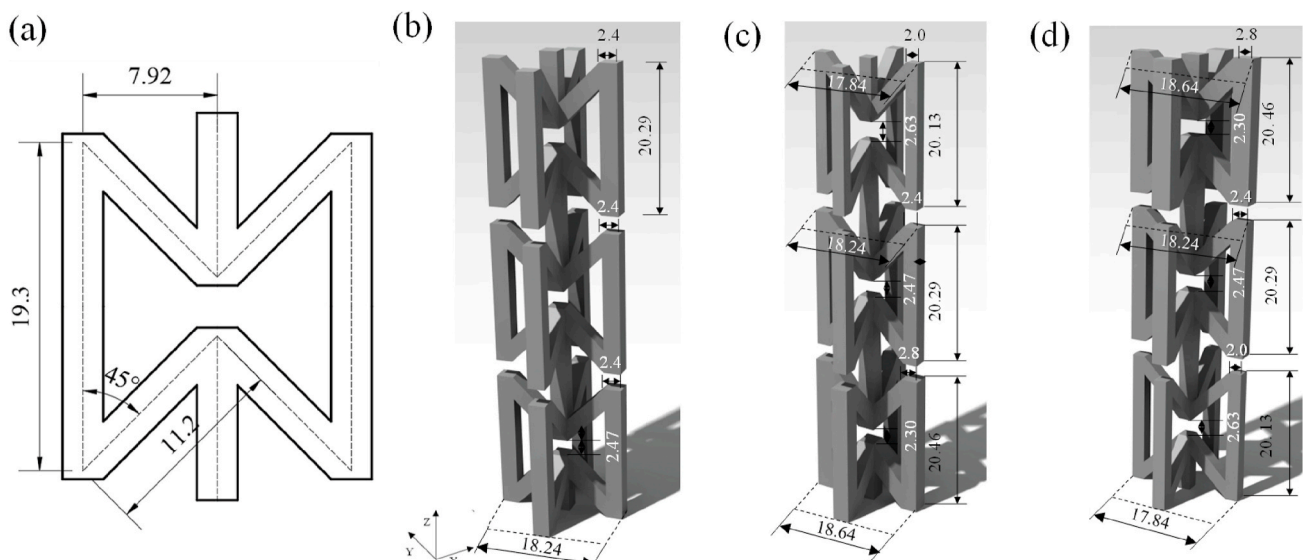


Fig. 1. Geometry of: (a) 2D unit cell, (b) 3D unit cell of U, (c) 3D unit cell of FG1, and (d) 3D unit cell of FG2 (unit: mm).

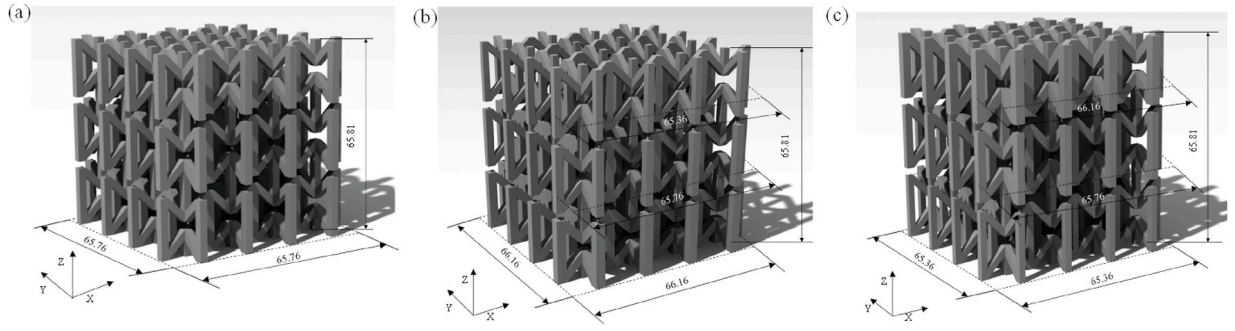


Fig. 2. Schematic illustration of (a) U, (b) FG1, and (c) FG2 (unit: mm).

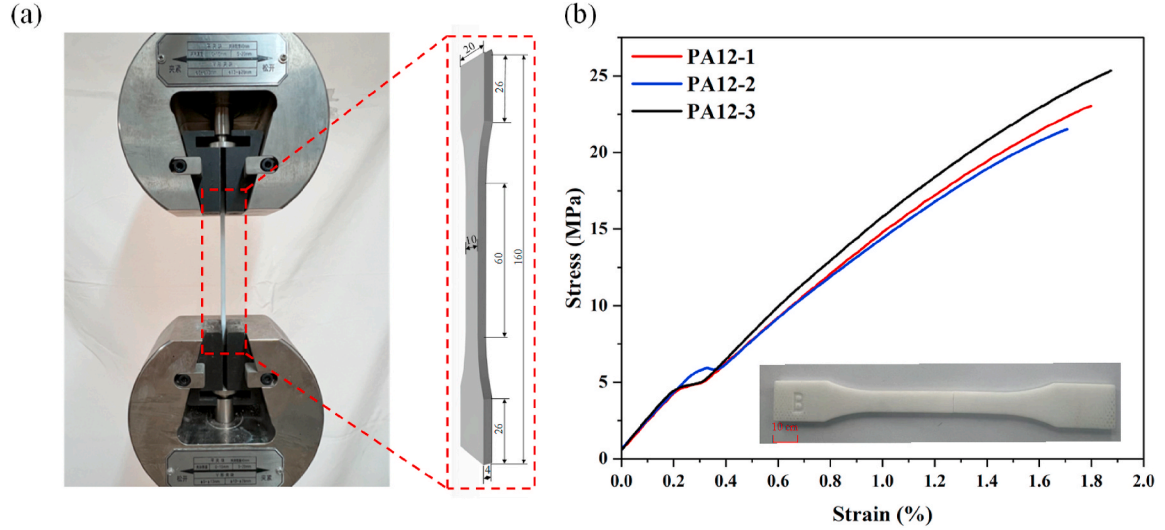


Fig. 3. Uniaxial tensile test on PA12: (a) test setup (unit: mm), and (b) tensile stress-strain curves.

symmetrically distributed at the corners on the left and right sides of each layer. The ruler placed beneath the bottom plate was used as the scale reference for distance measurements. To better identify the positions of reference points throughout the tests, all reference points were set at the intersections between the inclined and vertical struts, positioned close to the end of the vertical struts. The horizontal strain at reference points  $\varepsilon_{xi}$  can be obtained by:

$$\varepsilon_{xi} = \frac{A_{i0}B_{i0} - A_iB_i}{A_{i0}B_{i0}} \quad (1)$$

where  $A_{i0}B_{i0}$  stands for the original distance between reference points  $A_i$  and  $B_i$ ,  $A_iB_i$  denotes the distance of the following deformation ( $i = 1, 2, 3, 4, 5, 6$ ). The average transversal strain  $\varepsilon_X$ , longitudinal strain  $\varepsilon_Y$ , and Poisson's ratio  $\nu_{YX}$  at different layers of U, FG1 and FG2 structures can be derived as:

$$\varepsilon_X^{(n)} = \frac{\varepsilon_{X(2n-1)} + \varepsilon_{X(2n)}}{2} \quad (2)$$

$$\varepsilon_Y^{(n)} = \varepsilon_{\text{nominal}} \quad (3)$$

$$\nu_{YX}^{(n)} = -\frac{\varepsilon_X^{(n)}}{\varepsilon_Y^{(n)}} \quad (4)$$

where  $n$  represents the layer of lattice ( $n = 1, 2, 3$ ).

The compressive behaviour of HPC cubic specimens with a dimension of  $70.7 \times 70.7 \times 70.7 \text{ mm}^3$  was evaluated using a 3000 kN-range electro-hydraulic servo universal testing machine equipped with force gauges accurate to  $10^{-6} \text{ kN}$ , as per JGJ/T 70-2009 [45]. The specimen

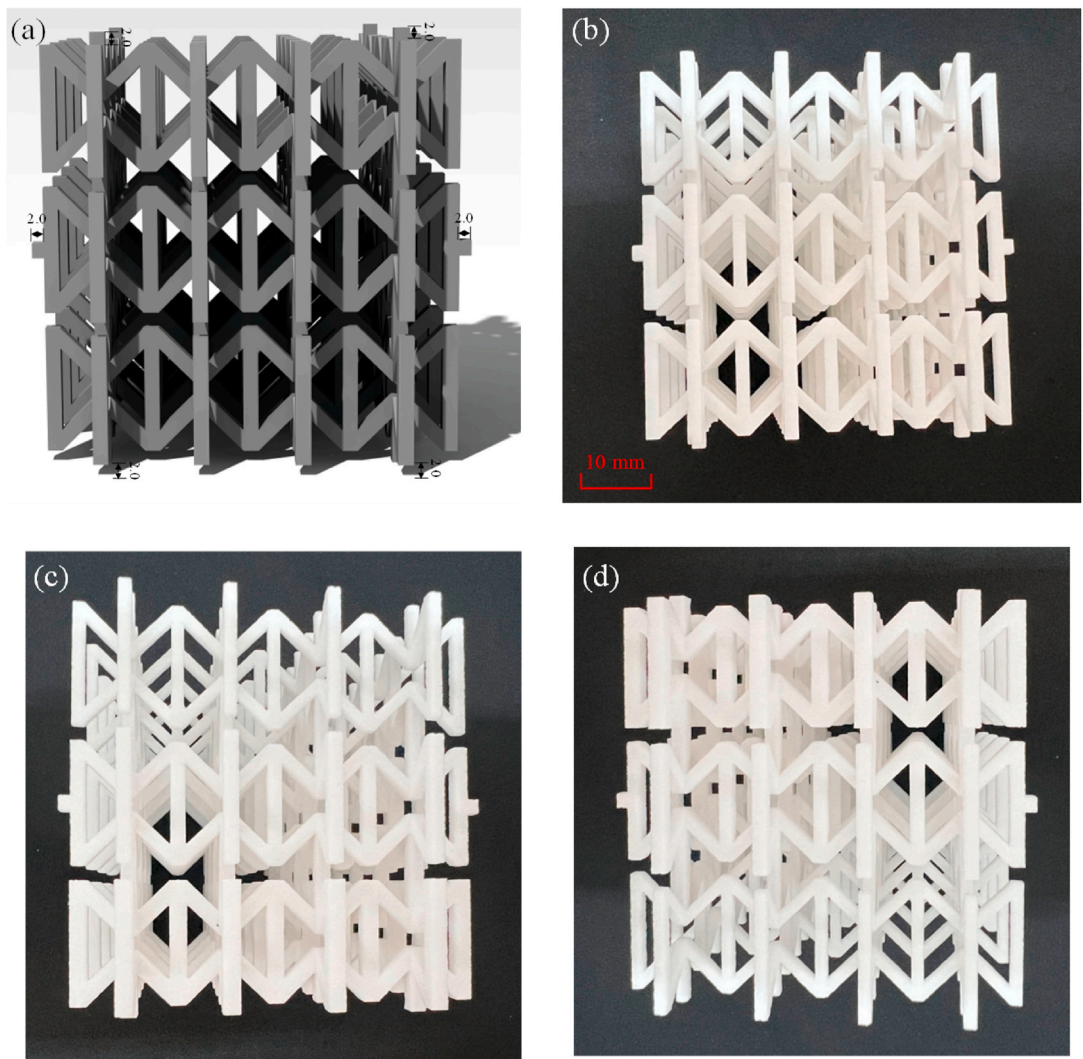
was placed on the lower platen of the testing machine. The load-bearing surface of the specimen should be perpendicular to the top surface during moulding process, with the centre aligning with the centre of the lower platen of the testing machine. The loading rate was constantly set as  $0.42 \text{ mm/min}$  to achieve quasi-static compression. The data including time, load and deformation were collected.

#### 2.4.2. Split Hopkinson pressure bar (SHPB) test

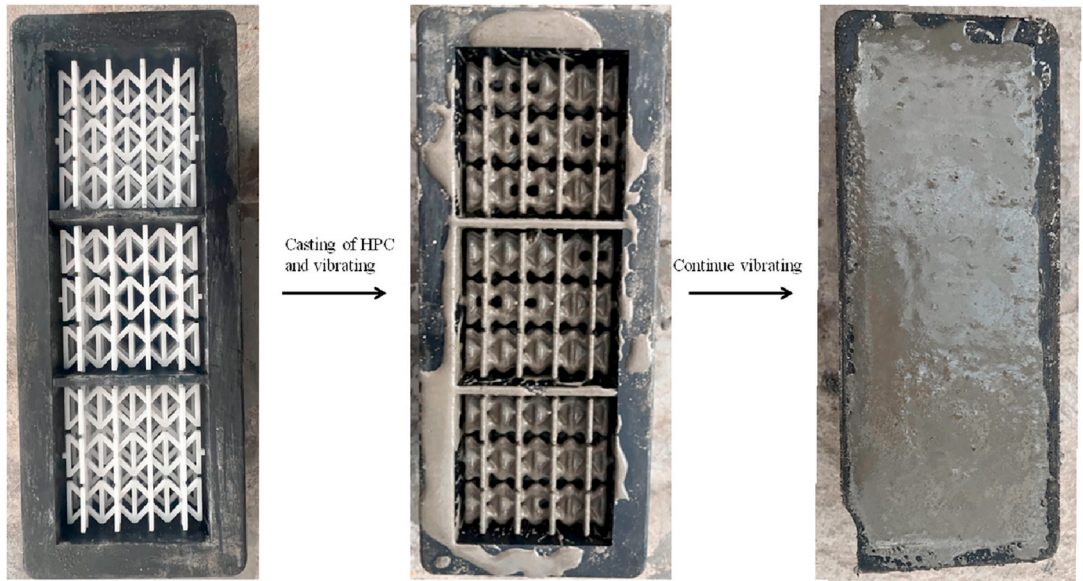
The dynamic compressive behaviour of four types of HPC specimens cured for 28 d was characterised using a SHPB system that was commonly employed to evaluate the dynamic performance of engineering materials subjected to high strain rates up to  $10^4 \text{ s}^{-1}$  [46]. As illustrated in Fig. 7, the alloy steel made SHPB apparatus consisted of a launch tube, a 5000 mm-length incident bar, a 3500 mm-length transmission bar, a 1200 mm-length absorbing bar and an absorber. The diameter of all bars is 100 mm, resulting in a maximum allowable diameter for all cubic specimens of 70.7 mm. A strike bar (with 600 mm in length) placed in the launch tube was adopted as a projectile to strike the incident bar. To collect and analyse the strain data, a digital oscilloscope and two strain gauges were introduced to the system. Particularly, the two strain gauges were symmetrically and tightly attached to the incident bar and the transmission bar, both of which were located at a distance of 2500 mm from the test specimens.

Prior to the test, the cubic HPC specimen with a diameter of 70.7 mm was clamped between the incident bar and transmission bar first. A thin layer of Vaseline was evenly applied to the specimen surfaces to minimise the interfacial friction. The acrylic container was fabricated to hold the specimen and prevent fractured concrete fragments from ejection.





**Fig. 4.** Illustration of 3D re-entrant lattices: (a) SLS printing model with protrusions, (b) 3D printed U sample, (c) 3D printed FG1 sample, and (d) 3D printed FG2 sample (mm).



**Fig. 5.** Casting and vibrating process for 3D re-entrant lattice reinforced HPC.

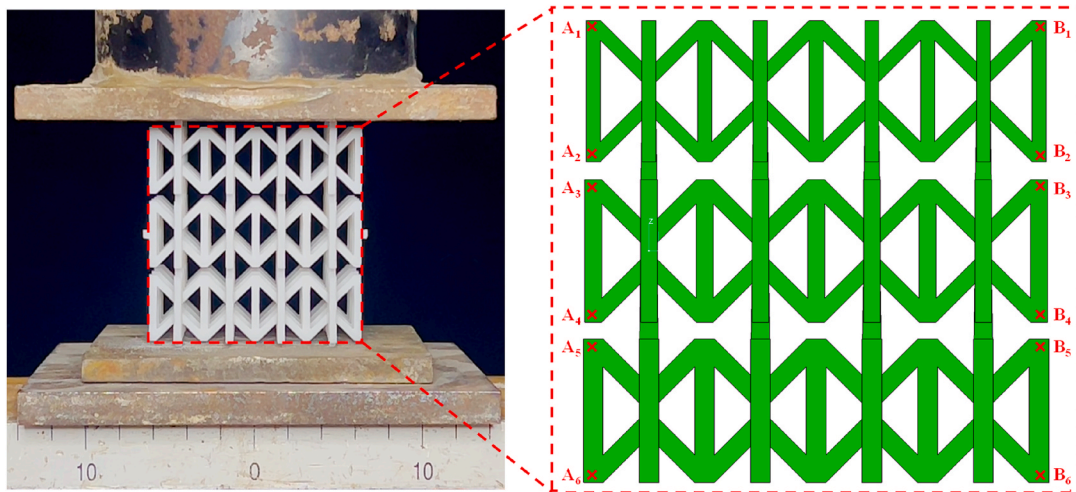


Fig. 6. Uniaxial quasi-static compressive test on 3D printed re-entrant lattice.

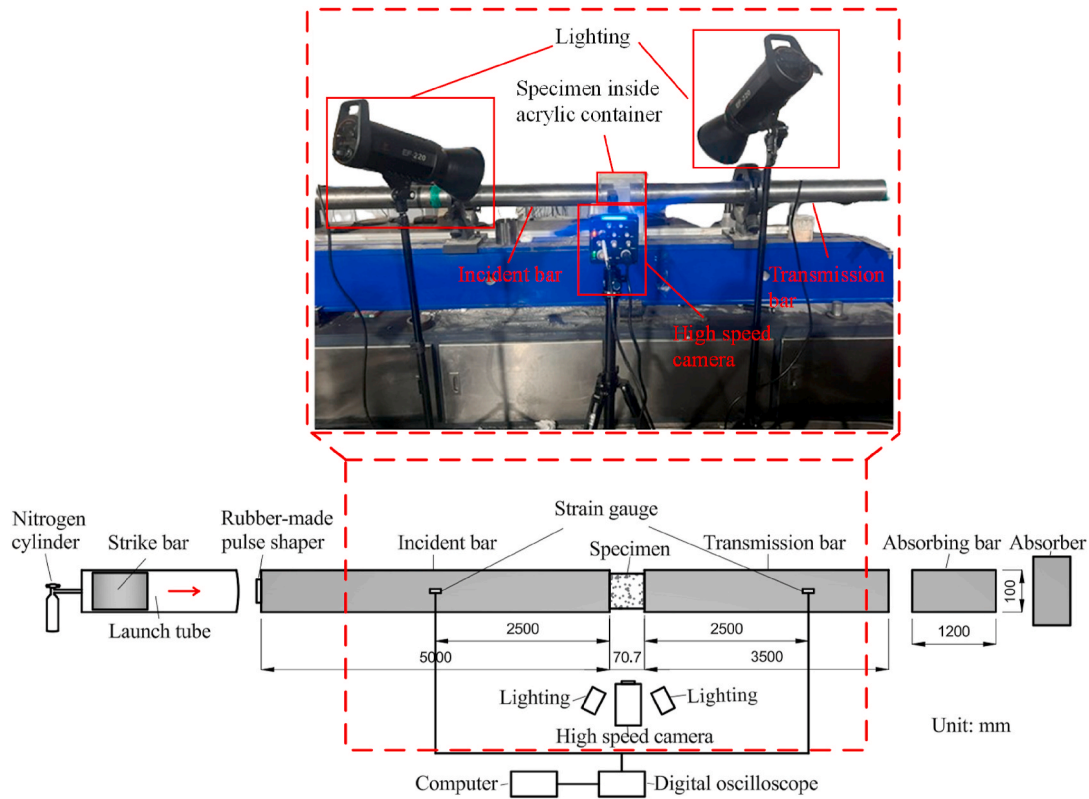


Fig. 7. Schematic illustration of SHPB test set-up.

The rubber-made pulse shaper (with diameter of 30 mm and height of 2 mm) was attached to the centre of the end of the incident bar, also known as the pulse shaping technique. Through extending the rising duration of the incident wave, the stress equilibrium could be achieved within the cubic specimen [47]. Moreover, the smooth of the incident curve directly reduced inertia and dispersion influence [48]. Thus, the accuracy of SHPB results was improved through the introduction of pulse shapers. An example for checking the stress equilibrium within the specimen is shown in Fig. 8. The projectile depth in the launch tube and the nitrogen gas pressure by computer should be regularly adjusted to achieve designed impact velocities, which can be measured by the speed detection device.

During the test process, the incident bar was first stroked by the

projectile, gradually producing the incident signal  $\varepsilon_I(t)$ . The incident wave arrived at front interface between the cubic specimen and the incident bar. The reflected signal  $\varepsilon_R(t)$  was generated by a portion of incident wave due to the impedance difference [49], along with the form of transmitted signal  $\varepsilon_T(t)$ , which continued to propagate into the transmission bar through the specimen. In theory, the strain rate and impact velocity of the same specimen exhibit a positive correlation relationship. Various strain rates (about  $30.0\text{--}100\text{ s}^{-1}$ ) were applied for P-HPC, U-HPC, G1-HPC and G2-HPC to ensure effective dynamic response of the specimens under low-energy impact conditions while reflecting practical applications involving typical hard engineering impact scenarios [50,51].

During the test, the incident signal  $\varepsilon_I(t)$ , reflected signal  $\varepsilon_R(t)$  and



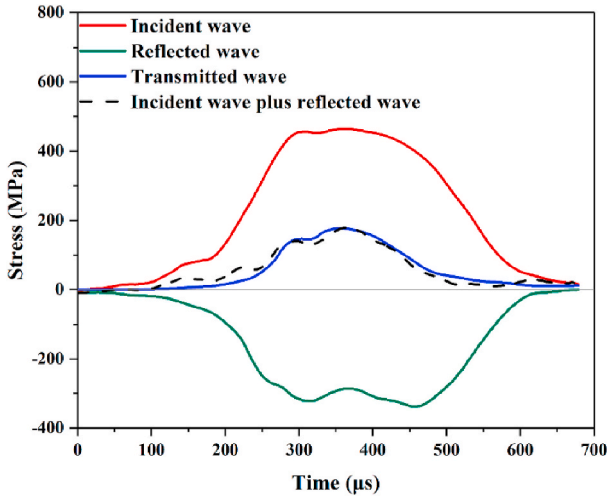


Fig. 8. A typical example for checking the stress equilibrium of the test specimen under impact loading.

transmitted signal  $\varepsilon_T(t)$  against time were obtained through digital oscilloscope to collect the strain signals from two strain gauges. Assuming the wave propagating in the bars is one-dimensional and elastic, and the axial stress and stress are both uniform in the testing specimen, the strain rate, strain and average stress of the test specimen can be determined as follows [46]:

$$\dot{\varepsilon} = \frac{c_0(\varepsilon_R(t) + \varepsilon_T(t) - \varepsilon_I(t))}{l} \quad (5)$$

$$\varepsilon = \frac{c_0}{l} \int_0^t c_0(\varepsilon_R(t) + \varepsilon_T(t) - \varepsilon_I(t)) dt \quad (6)$$

$$\sigma_s = \frac{A_b E_b (\varepsilon_I(t) + \varepsilon_R(t) + \varepsilon_T(t))}{2A_s} \quad (7)$$

where  $A_s$  denotes the cross-section area of the test specimen.

### 3. Results and discussion

#### 3.1. Static compressive behaviour of lattice structures

##### 3.1.1. Deformation patterns

Fig. 9 displays the deformation patterns of U, FG1 and FG2 structures during compression. The lateral translation of the middle layer and subsequent fracture of struts primarily took place in U structure, whereas FG1 and FG2 structures experienced a layer-by-layer collapse. For U structure, the entire structure initially exhibited tri-axial compression deformation as the strain increased from 0 to 10 %, with an obvious NPR effect. There was insufficient support on the neutral struts with a large aspect ratio, and the local deformation due to elastic instability tended to transfer to adjacent neutral struts [52]. In addition, the continuity, stability and coordination can be maintained as a whole owing to the compatibility restrictions of structure [53]. Hence, the middle layer underwent sudden lateral displacement in one direction. Then, the re-entrant struts and neutral struts gradually fractured at their weakest points due to shearing and bending. With the further increase of strain to 20 %, all connecting struts fractured, as a result of which the middle layer separated from the upper and lower layers. The unit cells in each layer closely adhered to that in the adjacent layers. As the strain went up to 40 %, the intermedium layer progressively collapsed, followed by the complete fracture and detachment of the struts. With the further increasing strain, the top and bottom layers started to collapse and compact with each other.

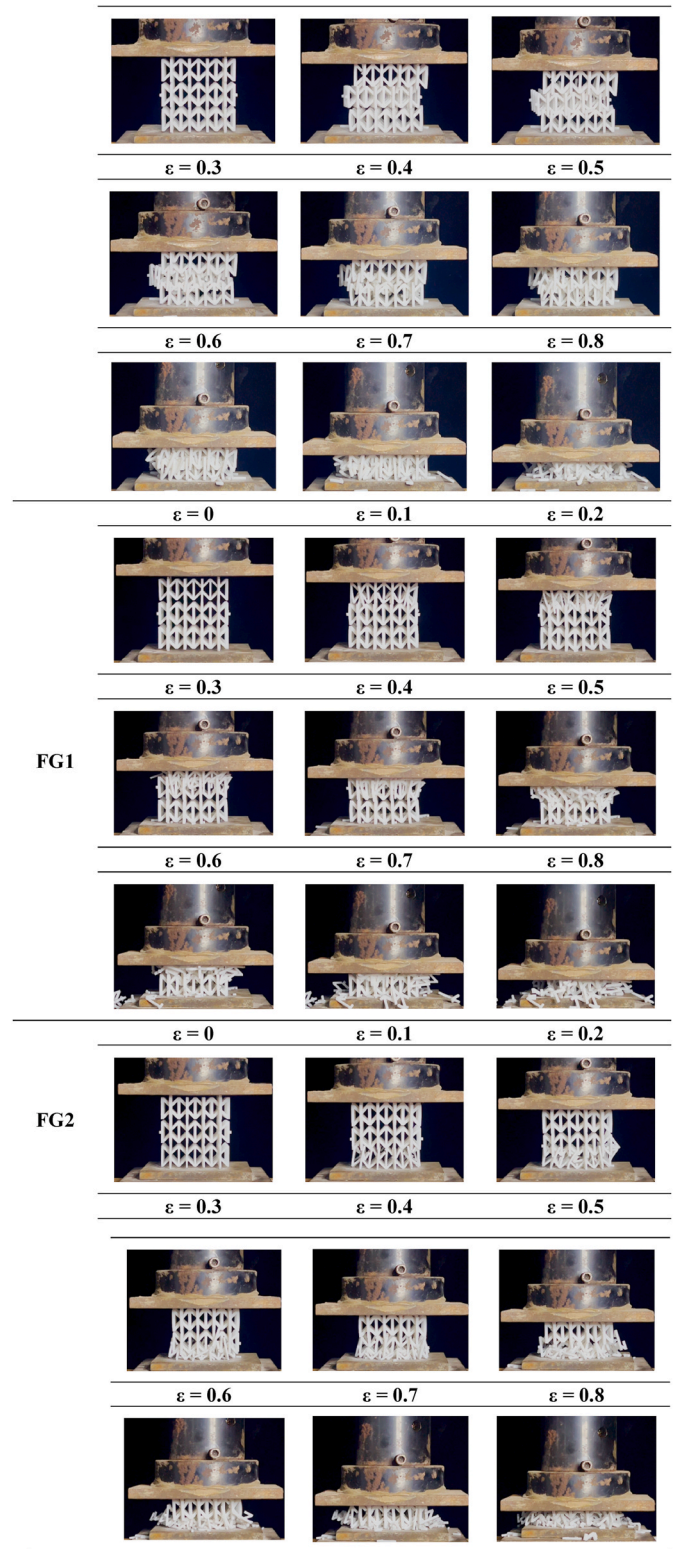


Fig. 9. Deformation patterns of U, FG1 and FG2 structures under static compression.

In contrast, graded structures presented a layer-by-layer collapse pattern. The incorporation of the functionally gradient design brought a more stable and controllable deformation [54]. For FG1 structure, the collapse progressed from the top layer with thinnest struts to the bottom layer. As the strain reached 10 %, a slight overall tri-axial contraction occurred in the whole structure, which was more pronounced in the top

layer. The compression of the vertical struts as well as the bending and shearing of the inclined struts were the primary deformations of the unit cell under ideal conditions [55]. The joints between the vertical and inclined struts of the unit cells moved inward under compression, and the fracture of the inclined struts initiated from the weakest points near the neutral struts. The unit cells in top layer twisted slightly, which can be attributed to the unbalanced bending moments on the neutral struts resulting from edge effects [53]. With the rise of strain to 20 %, the neutral struts connecting the top and middle layers gradually fractured under compression and bending. Thus, the top layer completely collapsed when the strain reached 30 %. The similar complete collapse process of middle and bottom layers can be observed when the strain was in the ranges of 30–60 % and 60–80 %, respectively. During this process, the fractured struts of the upper layers detached from the structure and the collapsed struts steadily contacted and compressed each other. Similarly, FG2 structure exhibited a progressive collapse from the bottom layer to the top layer, which occurred at the strain ranges of 10–30 %, 30–60 % and 60–80 %, respectively. During the layer-wise collapse process, the most obvious auxetic behaviour tended to appear in the layer with the thinnest struts.

### 3.1.2. Poisson's ratio

As seen in Fig. 10, all re-entrant structures exhibited significant NPR effects during static compressive process. With the increase of strain, the re-entrant angle ( $\theta$ ) gradually dropped, along with the reduction of horizontal displacement of the joints [56], leading to the decrease of transversal strain of the structure ( $\epsilon_x$ ) and absolute value of the average Poisson's ratio in each layer ( $\nu_{yx}^{(n)}$ ). This can be attributed to the increasing resistance of the re-entrant struts to horizontal deformation as strain increased. For U structure, the Poisson's ratios of the upper and lower layers followed a similar trend with strain before collapse, ranging from  $-0.38$  to  $-0.02$  and  $-0.41$  to  $-0.05$ , respectively. The middle layer also had a comparable Poisson's ratio at a strain of 5–20 %. However, the middle layer underwent a lateral displacement due to the large aspect ratio of neutral struts and edge effects (see Fig. 9). The premature local instability deteriorated the continuity and coordination of the whole structure, causing the NPR effects to only manifest in the early stage of compression.

In comparison, FG1 and FG2 had different Poisson's ratios across different layers with the increase of strain from 0 to 80 %. The boundary and torsional effects on unit cells across different layers during compression also contributed to the reduction in NPR effects for graded structures. The more pronounced NPR effects occurred in the layers with the thinner struts, which approximately twice that of the uniform structure. This can be explained by the fact that the thinner struts possessed lower resistance to bending and rotation, resulting in a greater relatively transversal deformation. The Poisson's ratios of FG1 varied

from the layer with the thinnest struts to the layer with the thickest struts as follows: from  $-0.79$  to  $-0.30$ , from  $-0.29$  to  $-0.03$ , and from  $-0.19$  to  $0$ , slightly lower than that of FG2 structures at the same strain which ranged from  $-1.07$  to  $-0.28$ , from  $-0.42$  to  $-0.03$ , and from  $-0.25$  to  $-0.02$ , respectively, as the contact layer directly subjected to external loads with thicker layer led to comparably higher load bearing capacity although under quasi-static loading.

### 3.1.3. Stress-strain responses

Fig. 11 presents the stress-strain curves of re-entrant structures under compression. The curves of U structure increased linearly until the neutral struts started to yield ( $\epsilon \approx 0-5$  %). Then, there was a rapid upward ascended to the initial peak stress (around 1.2 MPa), followed by a sharper decline caused by the fracture of neutral struts connecting middle layer with top and bottom layers and lateral translation of middle layer ( $\epsilon \approx 5-9$  %), which disrupted the structural stability, continuity and coordination, and thereby reducing the load-bearing capacity. The curve gradually increased with strain due to the contact and compression of the unit cells of different layers. With the further compression, the re-entrant, vertical and neutral struts were gradually broken at the weak joints, resulting in a sudden decline in stress. The progressive downward and upward fluctuation of the curve ( $\epsilon \approx 9-65$  %) indicated the continuous fracture of the struts and the subsequent

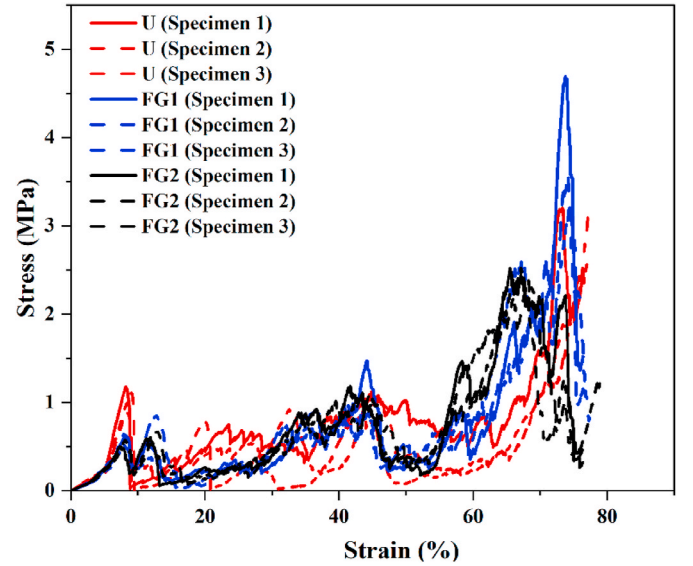


Fig. 11. Stress-strain curves of U, FG1 and FG2 structures under static compression.

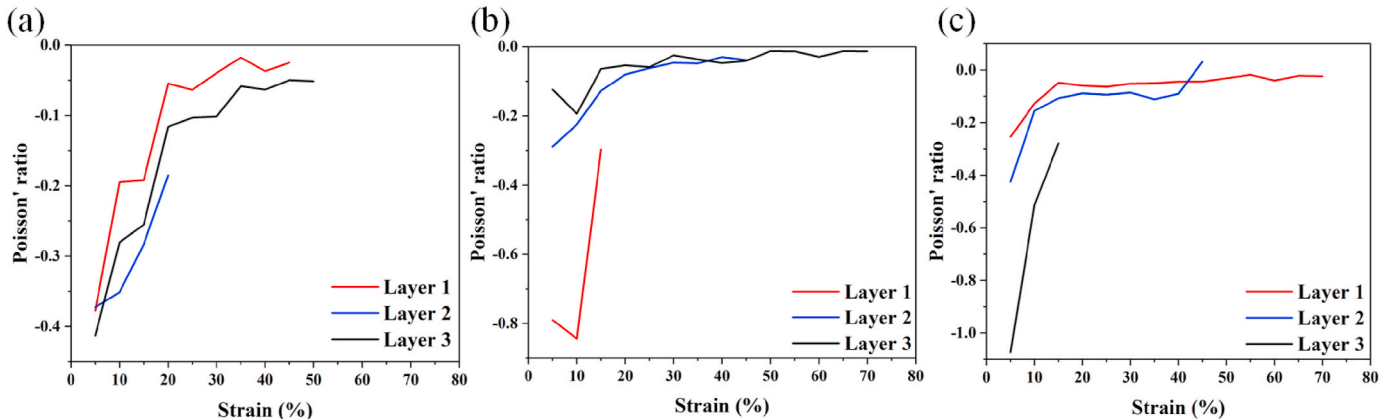


Fig. 10. Average Poisson's ratios of different layers in (a) U, (b) FG1, and (c) FG2 structures under compression.



compression of the other struts. Finally, the struts continued to break and compress each other, and thus the curve showed a steep upward trend ( $\varepsilon \geq 65\%$ ).

In contrast, the curves of FG1 and FG2 structures presented distinct stepwise trends. There was an elastic region first until the thinnest struts bent ( $\varepsilon \approx 0\text{--}3\%$ ), followed by three similar stages. The curves included the alternations of inclining, declining, and low-stress plateau stages ( $\varepsilon \geq 3\%$ ), which represented the progressive collapse and compaction in each layer from the weakest layer to the strongest layer. During the process of each stage, the compression of struts and the collapsed unit cells led to a rise in the stress, while the fracture and detachment of struts resulted in a loss in load-bearing capacity. This layer-by-layer collapse accompanied by a stress redistribution that reflected the effects of gradient design in controlling the deformation patterns and energy dissipation process.

As seen in Table 2, compared to U structure, FG1 and FG2 had 30.0 % and 9.5 % lower elastic modulus, 56.5 % and 47.8 % lower yield stress, 43.3 % and 47.9 % lower first peak stress, respectively. During initial compressive process, the thinnest struts in graded structures possessed lower stiffness and plastic resistance than that of equivalent U structure, leading to lower yield strength, elastic modulus and first peak stress [57]. However, with the increase of strain, the graded structure possessed higher stress in plateau stage. The step-like features of the graded lattices resulted in a higher load-bearing capacity with the increasing strain [27].

#### 3.1.4. Energy absorption

During the static compressive process, the PA12 struts could fracture and detach from the re-entrant structure, preventing the structures from reaching the theoretical densification stage through considering energy efficiency [58]. The energy absorption capacity of the lattice structure can be expressed as the integral of the stress-strain curve up to 80 % deformation [59]:

$$W_v = \int_0^{\varepsilon_0} \sigma d\varepsilon \quad (8)$$

where  $\varepsilon_0$  represents the target strain.

As seen in Fig. 12,  $W_v$  of U, FG1 and FG2 increased with strain until the strain reached around 80 %. The uniform structure exhibited significantly greater energy absorption than the graded structures in the early stages of deformation ( $\varepsilon \approx 0\text{--}37\%$ ). This was because the deformation and fracture of thicker struts in a uniform structure absorbed more energy under the same strain. Moreover, the uniform structure exhibited a more rapid overall collapse compared to graded structures. As indicated in Table 2,  $W_v$  of FG1 and FG2 was about 26.7 % and 19.2 % higher than that of U structure, respectively. Lattice structures were characterised by a flat plastic plateau region, associated with their geometric configuration [60]. The controllable deformation mode sourced from graded geometry is usually the main reason for the improved energy absorption capacity of the graded lattice compared to the uniform lattice [61]. The gradient design in FG1 and FG2 can cause more even stress distribution throughout the structure, slowing the deformation of struts and breaking of struts and allow more energy to be dispersed and absorbed up to densification.

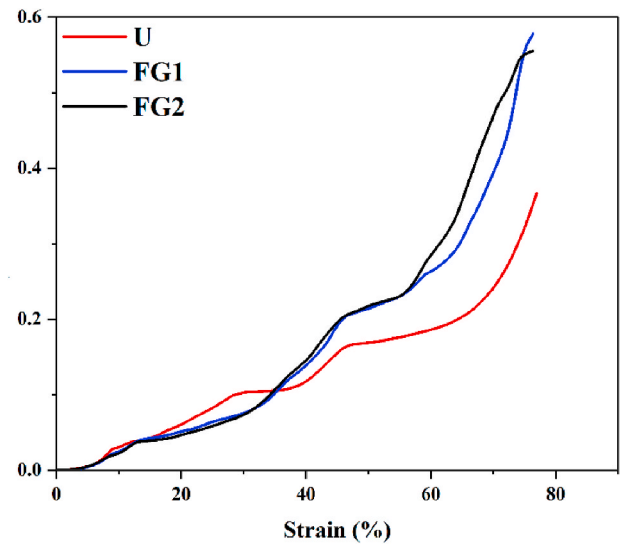


Fig. 12. Energy absorption for uniform and graded 3D re-entrant lattice structures under static compression.

### 3.2. Static compressive behaviour of composites

#### 3.2.1. Deformation patterns

Fig. 13 illustrates the cracking process of all HPC specimens with the increase of strains. The longitudinal cracks of P-HPC initially emerged and propagated from middle area of the specimens as the strain increased to around 1 %. Subsequently, with the progressive increase in strain, multiple cracks appeared on other surfaces, along with the further development of the existing cracks. When the strain reached around 3 %, a long longitudinal crack was formed, along with the spalling of the concrete surface. In comparison, the initial crack of U-HPC appeared longitudinally as the strain went up to 1 %. Then, the cracks further propagated and new cracks initiated on the border of the surface, followed by gradual spalling of concrete on the lateral surface with the further rise of strain to around 3 %. The diagonal cracks developed on the concrete surface due to the friction on the end face under compression [62]. The matrix underwent further cracking, while the internal struts maintained a certain load-bearing capacity, continuing to bear the load until the complete spalling of the outer concrete on the surface ( $\varepsilon \approx 8\text{--}10\%$ ). Different from U-HPC, the initial longitudinal cracks appeared in the upper part of G1-HPC. The weak struts in the upper layer made cracks more likely to occur in the critical position. Correspondingly, the initial crack of G2-HPC appeared at the bottom border of the composite as the strain reached around 2–3 %, followed by the occurrence of longitudinal cracks. Both G1-HPC and G2-HPC experienced gradual development of multiple longitudinal and diagonal cracks on the surface when reaching the ultimate compressive strength, and then progressive spalling of concrete with the further increase of strain ( $\varepsilon \approx 4\text{--}10\%$ ). Although the lattice reinforced cementitious composites still exhibited brittleness [6], the overall cracking development was hindered of lattice reinforced HPC specimens with the increase of strain. A triaxial compression of matrix could be formed during the compression sourced from the NPR effects of 3D re-entrant lattice reinforcement, which inhibited the initiation and propagation of micro-cracks. The crack propagation and spalling of concrete of

Table 2  
Mechanical properties of different lattice structures under static compression.

Specimen	Elastic modulus (MPa)	Yield stress (MPa)	First peak stress (MPa)	Strain at first peak stress (%)	Energy absorption up to 80 % deformation (MJ/m <sup>3</sup> )
U	4.53 ± 0.45	0.23 ± 0.02	1.06 ± 0.16	8.53 ± 0.45	0.45 ± 0.11
FG1	3.17 ± 0.28	0.10 ± 0.01	0.60 ± 0.07	7.98 ± 0.18	0.57 ± 0.05
FG2	3.19 ± 0.80	0.10 ± 0.01	0.55 ± 0.04	7.85 ± 0.48	0.54 ± 0.02

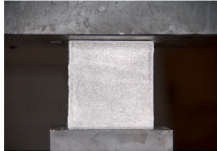
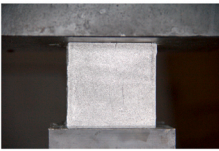
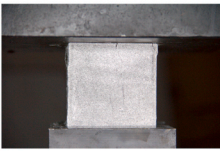
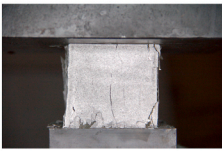
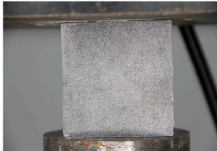
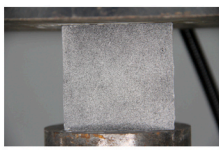
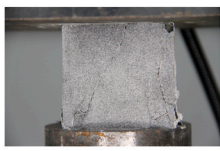
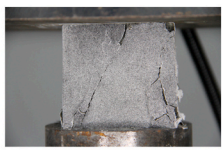



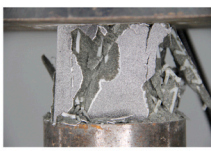
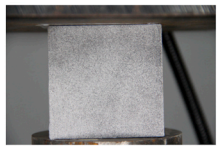
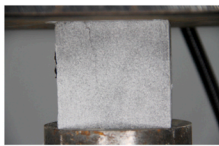
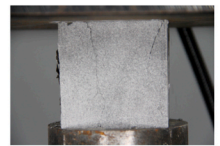
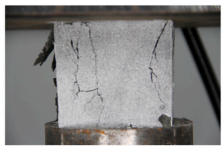
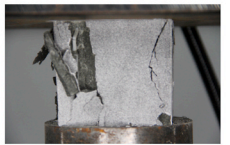
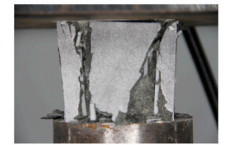
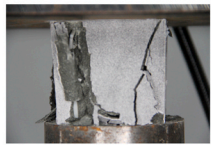

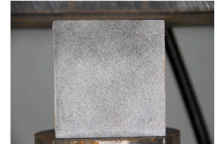
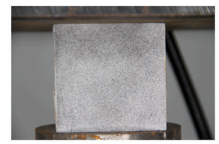
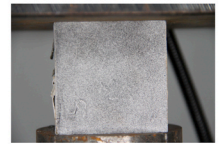
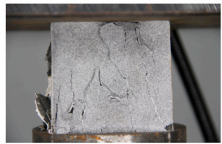
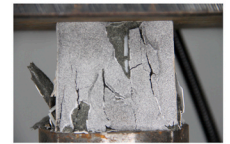
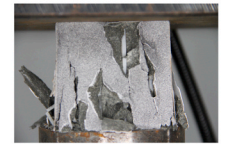


Sample	Strain and corresponding failure pattern			
	$\varepsilon = 0$	$\varepsilon = 0.01$	$\varepsilon = 0.02$	$\varepsilon = 0.03$
P-HPC				
	$\varepsilon = 0$	$\varepsilon = 0.01$	$\varepsilon = 0.02$	$\varepsilon = 0.03$
				
	$\varepsilon = 0.04$	$\varepsilon = 0.06$	$\varepsilon = 0.08$	$\varepsilon = 0.10$
U-HPC				
	$\varepsilon = 0$	$\varepsilon = 0.01$	$\varepsilon = 0.02$	$\varepsilon = 0.03$
				
	$\varepsilon = 0.04$	$\varepsilon = 0.06$	$\varepsilon = 0.08$	$\varepsilon = 0.10$
G1-HPC				
	$\varepsilon = 0$	$\varepsilon = 0.01$	$\varepsilon = 0.02$	$\varepsilon = 0.03$
				
	$\varepsilon = 0.04$	$\varepsilon = 0.06$	$\varepsilon = 0.08$	$\varepsilon = 0.10$
G2-HPC				

Fig. 13. Cracking processes of HPC specimens under static compression.

graded lattice reinforced HPC were more severe than U-HPC, as the localised damage of the concrete matrix and fracture of struts could occur in the weak area with thinner struts due to stress concentration.

Fig. 14 displays the failure patterns of re-entrant lattice reinforced HPC specimens. It can be observed that the outer struts were more prone to localised damage and severe fracture in critical positions as the re-entrant lattice reinforced HPC failed, leading to the spalling of concrete reinforced by the outer unit cells. Similar to the re-entrant honeycomb lattice reinforced UHPC, the cracks of all re-entrant lattice reinforced HPC specimens tended to develop along the vertical struts [16]. The weak reinforcement at the joints of the re-entrant and vertical struts was conducive to the cracking development. As seen in Fig. 14b–c, the cracks in upper layer of G1-HPC and the bottom layer of G2-HPC were wider than that of U-HPC. The reinforcement effects induced by the weaker layer in graded lattice reinforced HPC caused cracks to develop more easily in the initial stages as compared to uniform composites. Meanwhile, it can be clearly observed that the compression and localised damage of the weakest layer in the graded lattice reinforced HPC were more severe than that of the other two layers due to stress concentration. However, the overall integrity of G1-HPC and G2-HPC after compression was higher than that of U-HPC, and the controllable and predictable failure modes were important advantages during the compression of concrete.

### 3.2.2. Stress-strain responses

Fig. 15 presents the compressive stress-strain curves of HPC specimens. Firstly, the curves of all specimens exhibited a nearly linear increase as the strain increased. Then, only P-HPC experienced immediate failure at a strain of around 2.8 % upon reaching the peak stress. The stress-strain curves of 3D re-entrant lattice reinforced HPC specimens displayed a different trend: a shifting ascent to peak stress, followed by a gradual strain-softening stage and then a sustained stress plateau stage at around 20 MPa, after the strain of 10 %. The embedded continuous lattice structures could support stress transferring and re-distribution to mitigate stress concentration after matrix cracking within concrete, providing supplementary support to encourage increased plastic deformation as opposed to the inherent brittle failure of P-HPC [63,64]. Furthermore, similar to biaxial compression of polymer materials reinforced by 2D re-entrant structure [25], the hardened concrete could be uniformly divided into sections by 3D re-entrant lattice confinement, with each section subjected to triaxial compression. The mechanical properties of HPC specimens were improved combining the augmented confinement effects with the inherent high compressive strength of concrete [12]. Hence, the enhanced post-peak load capacity of 3D re-entrant lattice reinforced HPC provided significantly excellent structural resilience and damage tolerance, enabling the composites to mitigate brittle failure and absorb more strain energy. Compared with U-HPC, G1-HPC and G2-HPC had relatively more smooth declining curves, indicating that the development of cracks and enlargement of zone damage can be delayed by stiffer layer of graded lattices. The strain at the peak stress of U-HPC was largest (i.e., 3.6 %), followed by G2-HPC (3.3 %), G1-HPC (3.0 %) and P-HPC (2.8 %). This can be explained by the fact that concrete underwent local plastic deformation in regions

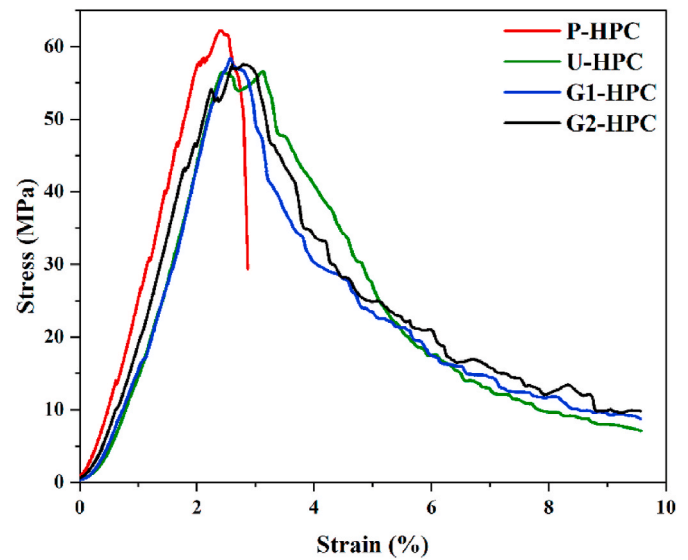


Fig. 15. Stress-strain curves of HPC specimens with/without lattice reinforcement under static compression.

with thinner struts, leading to premature failure.

### 3.2.3. Compressive strength

Fig. 16 illustrates the compressive strength of HPC specimens. P-HPC exhibited the lowest compressive strength of 59.9 MPa, which was 0.3 %, 5.8 % and 3.9 % lower than U-HPC, G1-HPC and G2-HPC, respectively. The compressive strength of re-entrant lattice reinforced HPC

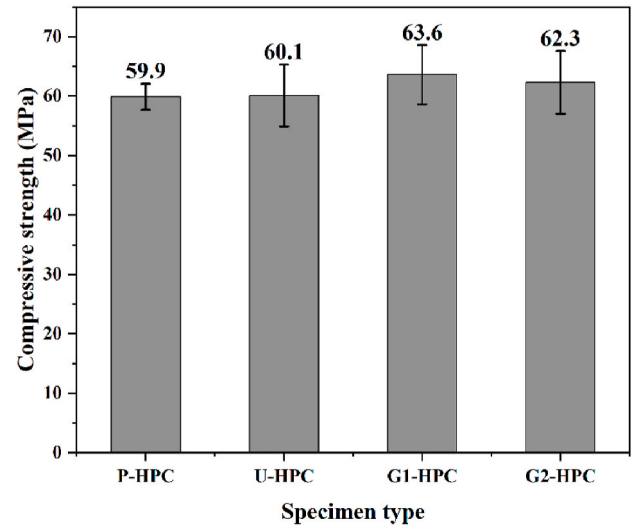


Fig. 16. Static compressive strength of HPC specimens.

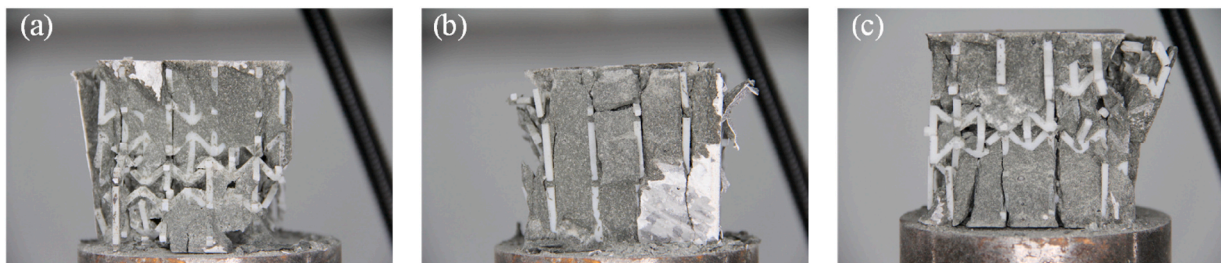


Fig. 14. A comparison of failure patterns of (a) U-HPC, (b) G1-HPC, and (c) G2-HPC under static compression.



specimens was slightly improved, indicating that the additional support from lattice reinforcement can lead to an enhanced load-bearing capacity of HPC [65]. Moreover, the internal 3D re-entrant lattices contracted inward from the other two directions under compression to achieve a tri-axial compression state of HPC matrix, which can be regarded as augmented confinement [12]. However, there was a significant strength difference between the lattice material and HPC, resulting in a weakening of the reinforcement effect. The compressive strength of graded lattice reinforced HPC was slightly higher than that of U-HPC. As compared with uniform lattice reinforcement, graded lattice tended to have more significant NPR effects in the layer with thinner struts, resulting in more effective augmented confinement on cementitious composites.

### 3.2.4. Dissipated energy

The energy dissipation of lattice reinforced concrete under compression consisted of the energy dissipated by both concrete and reinforcement, which can be obtained by the sum of area under the load-displacement curve. Fig. 17 shows the dissipated energy of HPC specimens until the strain reached around 10 %. The re-entrant lattice reinforced HPC had much higher energy dissipation until failure due to the sustained strain-softening stage after peak stress compared to P-HPC without lattice reinforcement. To clarify the actual energy dissipation capacity of cementitious composites with different recovery elastic energy absorption capacity, the plastic dissipated energy defined as the difference between total energy and elastic strain energy was employed [66,67]. The irreversible plastic energy mainly included the energy dissipated through plastic deformation, microcracking, fracture of struts, interfacial friction, debonding and sliding between concrete and lattice. The plastic stage of the specimens generally began at a strain of around 0.6–0.7 %, after which the plastic dissipated energy of P-HPC reached 346.5 J, which was 57.0 %, 54.6 % and 58.7 % lower than that of U-HPC, G1-HPC and G2-HPC, respectively. The auxetic lattice reinforcement in HPC ensured the bonding between concrete and lattice and kept residual stresses after the crack formation. The lattice reinforcement providing active triaxial confinement for concrete continued to redistribute stress across the entire specimen and reduce the stress concentration after the initiation of microcracks within concrete. The plastic deformation after peak stress can be greatly improved although concrete gradually lost load-bearing capacity with increasing strain. Moreover, the lattice reinforcement caused stress distribution across the entire sample, offering supplementary support to encourage increased plastic deformation although concrete lost load-bearing capacity. The reinforcement kept the specimen remained together under large axial

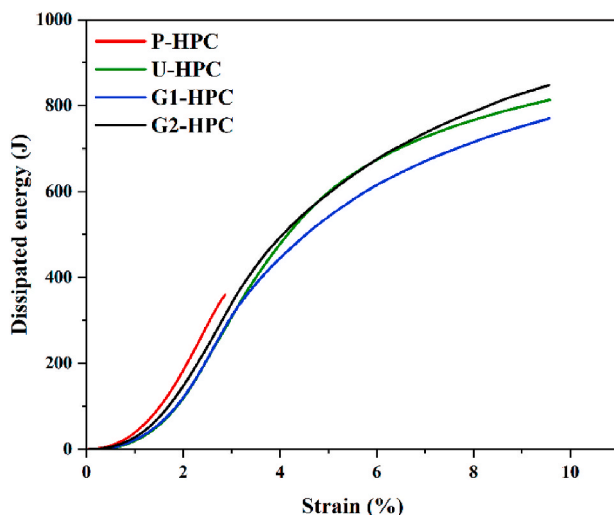


Fig. 17. Dissipated energy of HPC specimens.

strains and offered support to concrete to absorb energy through tensile elongation and fracture of struts during compression [16]. The lattice reinforced HPC had superior similar energy absorption capacity through high residual strength and ductility, showing a great potential in protective structures.

### 3.3. Dynamic compressive behaviour of composites

#### 3.3.1. Failure patterns

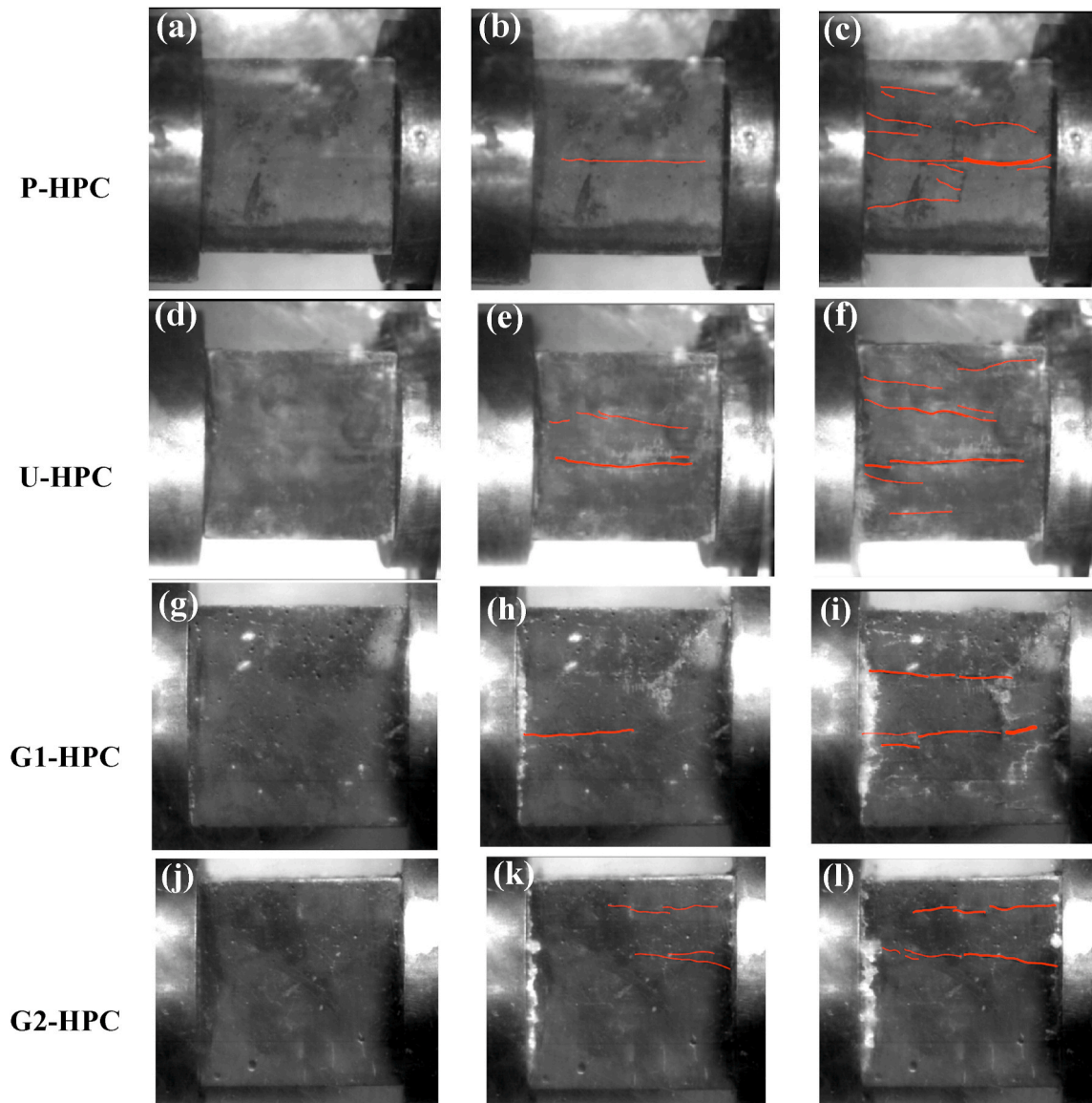
Fig. 18 displays the crack development of HPC specimens under similar strain rates (around  $72 \text{ s}^{-1}$ ). The four specimens underwent similar trends: the main longitudinal cracks could form in the middle or near the edge, along with the appearance of multiple observable cracks around the main crack (Fig. 18b–e, h and k). Then, the existing cracks would grow, while one or more longitudinal cracks could be generated (Fig. 18c–f, i and l). This is because the short impact loading duration prevented the development of existing micro-cracks and allowed formation of new micro-cracks [68]. Finally, the rapid development of cracks caused the ultimate failure of the specimens. During this process, the inclined cracks could appear on the surface and propagate into the longitudinal direction, which can be attributed to the pre-existing defects in HPC specimens [69]. Similar to P-HPC, the cracks of lattice reinforced HPC also developed parallel to the direction of the dynamic compression as the weak joints of the lattice reinforcement were arranged longitudinally.

As seen in Fig. 19 for the failure patterns of all HPC specimens under dynamic compression, with the increasing strain rate from around  $28.1 \text{ s}^{-1}$  to  $100.6 \text{ s}^{-1}$ , the failure patterns of P-HPC changed from keeping almost no damage to small fragments failure. Slight perpendicular cracks can be observed in P-HPC at a strain rate of around  $28.1 \text{ s}^{-1}$  (Fig. 19a), followed by rapid crack propagation and damage of the edge portions into large pieces as the strain rate increased to around  $50.6 \text{ s}^{-1}$  due to brittleness of HPC (Fig. 19b). With the further increase of strain rate, the specimens progressively damaged into large fragments without distinct main portions (Fig. 19c). At around  $100.6 \text{ s}^{-1}$ , the size of the fragments became smaller (Fig. 19d). The progression of failure modes with the increase of strain rates was consistent with that in other plain concrete under dynamic compression [70,71].

In comparison, the 3D re-entrant lattice reinforced HPC experienced distinct damage evolution at similar strain rates: changing from the almost intact specimens with cracks and slight concrete spalling to large main portions with small fragments. At around  $28.1 \text{ s}^{-1}$ , U-HPC, G1-HPC and G2-HPC all had perpendicular cracks on the surface (Fig. 19e–i and m). The concrete between the outer unit cells was prone to spalling slightly at edges without internal lattice reinforcement. When the strain rate reached around  $50.6 \text{ s}^{-1}$ , multiple wider and longer cracks were developed along the vertical struts in all lattice reinforced HPC specimens, while the slight concrete failed at the edges of impact surface (Fig. 19f–j and n). Compared to graded lattice reinforced HPC, a penetrating crack can be observed within the specimen for U-HPC, ascribed to the stronger layers in graded lattice structures with greater strength under dynamic compression, which prevented the weaker joints from completely breaking at low strain rates. With the increase of strain rate to around  $72.0 \text{ s}^{-1}$ , more cracks formed on the surface and developed inward, as a result of which the lattice reinforced HPC specimens were transformed into several main sections. Meanwhile, a few outer unit cells detached in alignment from the main sections. The crack initiation and propagation along the vertical struts of lattices were more pronounced, consistent with the failure patterns in static compression. The stress concentration at weak joints of the re-entrant and vertical struts sourced from uneven stress transfer was conducive to the cracking development. At around  $100.6 \text{ s}^{-1}$ , U-HPC, G1-HPC and G2-HPC kept certain main sections, followed by the vertical fragments detaching in alignment along the weak joints.

Under lower strain rates (below around  $30 \text{ s}^{-1}$  in this study), lattice reinforced HPC tended to exhibit a few more severe damages than P-





**Fig. 18.** Crack development of HPC specimens at a similar strain rate of  $72 \text{ s}^{-1}$  (red lines denote cracks, and their thickness indicates the crack width). (For interpretation of the references to colour in this figure legend, the reader is referred to the Web version of this article.)

HPC, which was mainly reflected in the crack development and slight concrete spalling (Fig. 19a–e, i and m). This can be explained by the fact that the stress concentration could occur in some areas, especially the weak joints connecting the re-entrant struts with neutral struts and vertical struts in lattice reinforced HPC specimens due to the geometric discontinuity [55,72]. Meanwhile, the geometric limitation of the lattices resulted in a lack of effective confinement on the external concrete between the outer unit cells, causing part concrete portions at the edges to spall due to the propagation of cracks. However, as the strain rate went up to around  $50.6 \text{ s}^{-1}$ , the lattice reinforced HPC had fewer fragments and better integrity under impact. Similar to other reinforcements, the 3D re-entrant lattices could restrict the lateral deformation of inside matrix under dynamic compression [73]. Moreover, the NPR effects of 3D re-entrant lattice reinforcement caused the internal concrete simultaneously experiencing inward compression in the other two directions from struts under compression [12]. Such augmented confinement effect enhanced the dynamic compressive resistance and delayed the development of internal cracks under high-speed impact.

The plain concrete specimens presented different cracking

development compared to lattice reinforced HPC. As seen in Fig. 19, P-HPC without lattice reinforcement had multiple penetrating cracks at a strain rate of around  $50 \text{ s}^{-1}$ . In contrast, for U-HPC specimens, although vertical cracks propagated along the vertical struts from top to bottom, the lattice reinforcement prevented the rapid formation of penetrating cracks, as shown in Fig. 20. During the dynamic compressive process, microcracks may initiate within the lattice unit cells, while the propagation was restricted by the multidirectional confinement.

### 3.3.2. Stress-strain curves

Fig. 21 shows the stress-strain curves for all HPC specimens at various strain rates varying from  $25.1 \text{ s}^{-1}$  to  $106.4 \text{ s}^{-1}$ . Most of specimens followed the similar trends, starting with a nearly linear elastic region, followed by a short plastic region, a fluctuating region, and finally a rapid decline until failure. Damage was crucial to the dynamic compressive response of HPC specimens during the process, especially to the peak stress in the stress-strain curves [69]. The short plastic region after elastic stage can be explained by the initiation and propagation of micro-cracks. Due to strain rate effect, the specimens had higher dynamic compressive strength but unstable post-peak failure (fluctuating

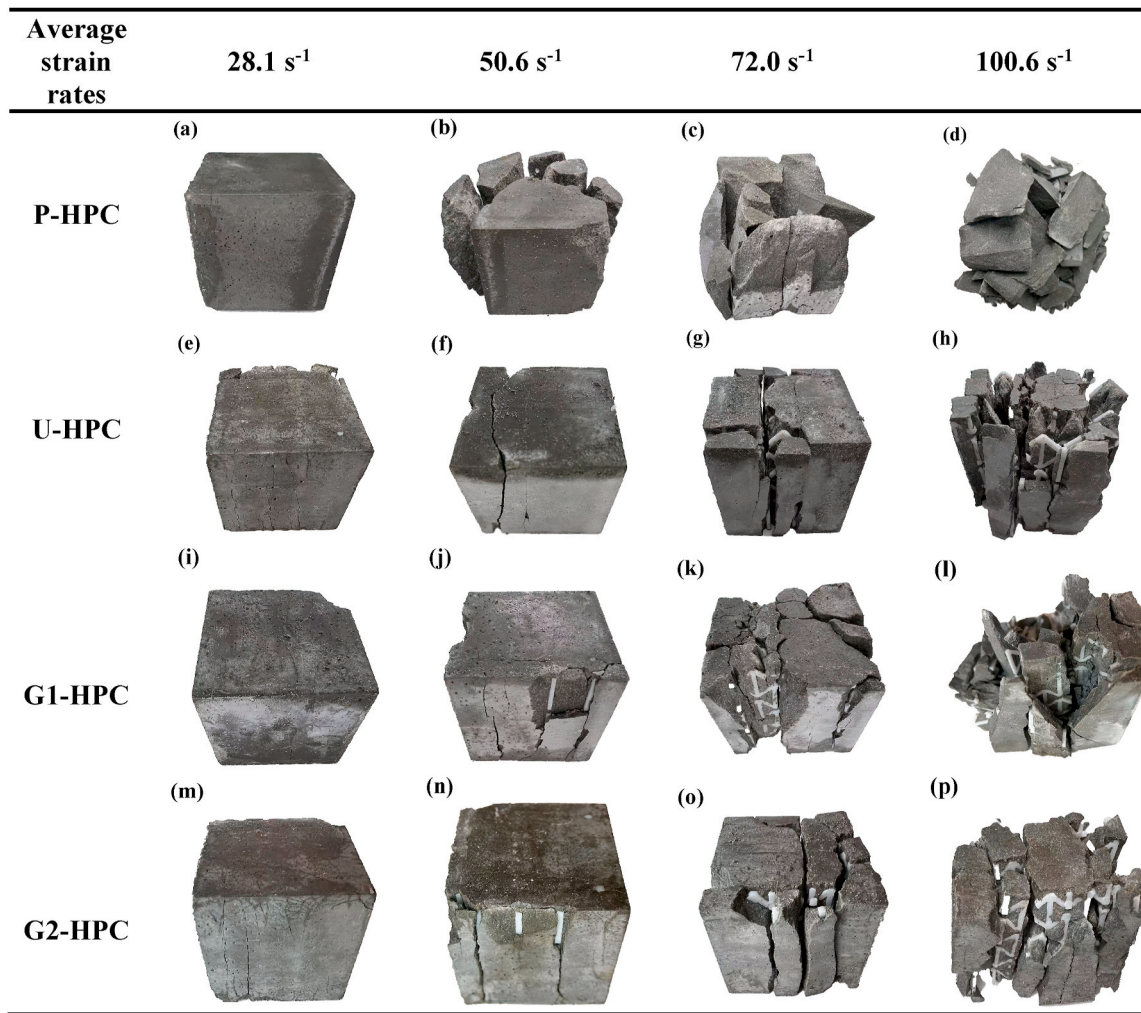


Fig. 19. Failure patterns of different specimens at various strain rates.



Fig. 20. Internal cracks of U-HPC at a strain rate of around 50 s<sup>-1</sup>.

stage), different from the pre-peak response [74]. During the fluctuating stage, the declining segment denoted the internal large cracks, localised damage, fragmentation and granular flow in the specimens [75]. The inclining segment may be ascribed to the tighter contact between the aggregates and the rising internal pressure induced by lateral confinement during dynamic loading [76], as a result of which part microcracks closed tightly, leading to a rebound in the localised strength and increase

in stress. Meanwhile, for lattice reinforced HPC, the active confinement effect also led to multiaxial compression of concrete, along with a rebound in stress.

A summary of dynamic compressive properties of all HPC specimens under various strain rates is given in Table 3, indicating a rise of dynamic compressive strength of all HPC specimens with the increase of strain rates. Compared to static compressive strength, the dynamic compressive strength of P-HPC, U-HPC, G1-HPC and G2-HPC was respectively about 86.3–154.3 %, 49.1–147.1 %, 57.7–160.5 %, and 44.6–218.3 % higher, ascribed to the rapid increase of the external energy under impact when the strain rates went up, which resulted in the formation and growth of micro-cracks. However, the short impact loading duration prevented the existing micro-cracks from propagating and thereby causing the specimens failure, with the formation of a large number of new micro-cracks [68]. The increased strain energy in the specimens could be mainly dissipated by the formation of cracks, leading to higher dynamic compressive strength [3,71]. Owing to the Stefan effect, the free water inside the concrete could hold resistance to compression, which tended to rise with the increase of strain rates [51]. The strength enhancement of HPC can also be attributed to the inertia effects under dynamic compression [77,78]. Concrete specimens had not enough time to adapt to the impact due to the short loading duration. The inertial force tended to resist the lateral deformation induced by impact loading and HPC specimens were in a triaxial compressive stress state, thereby enhancing the dynamic strength [79]. The lateral confinement resulted from the interface of specimens and restriction of

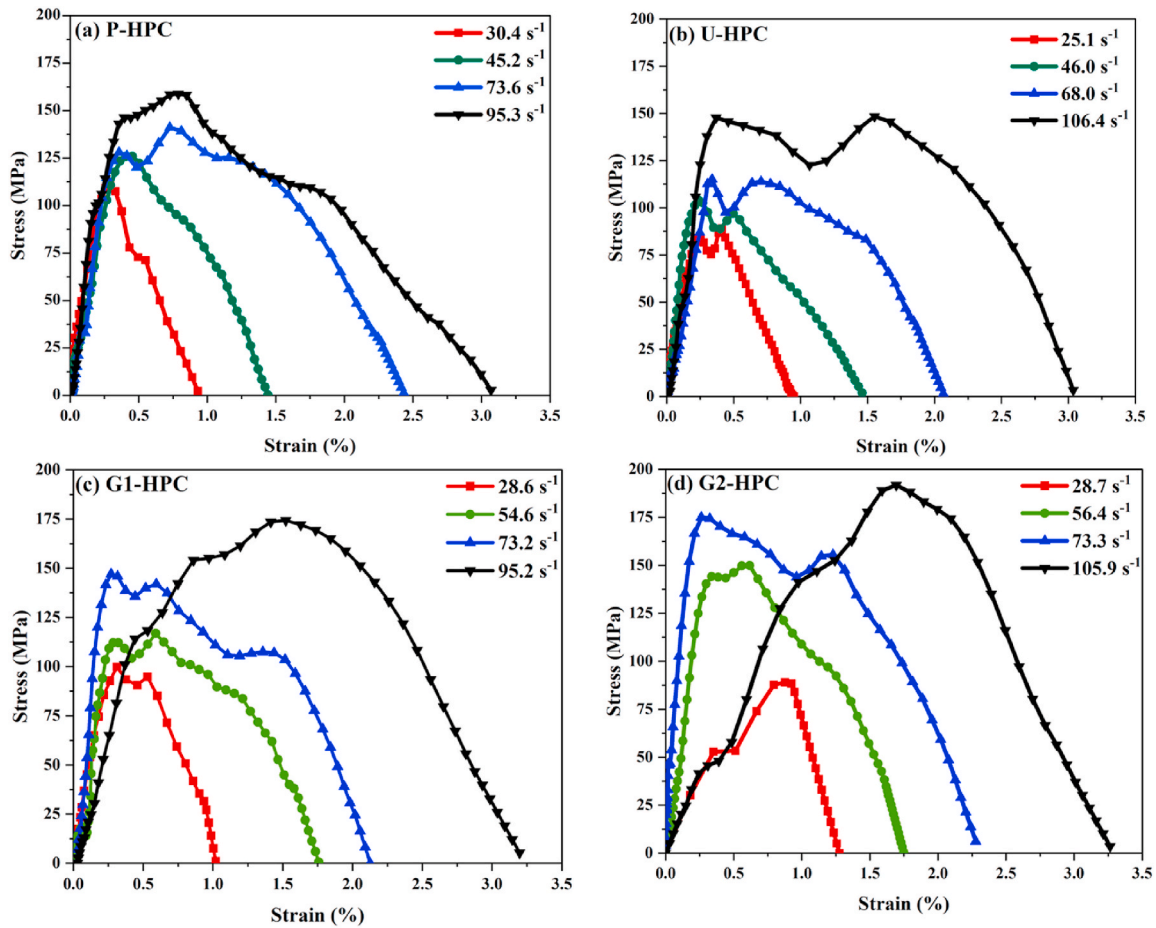


Fig. 21. Effect of strain rate on dynamic compressive stress-strain curves of (a) P-HPC, (b) U-HPC, (c) G1-HPC, and (d) G2-HPC.

Table 3

Summary of dynamic properties of all specimens obtained from SHPB test.

Symbol	Strain rate (s <sup>-1</sup> )	Dynamic compressive strength (MPa)	DIF	Ultimate strain (× 10 <sup>-3</sup> )	Total energy (J)
P-HPC	30.4	111.6 ± 4.8	1.86 ± 0.080	9.44 ± 2.18	130.3 ± 7.6
	45.2	121.4 ± 7.6	2.03 ± 0.127	12.04 ± 1.43	328.9 ± 9.8
	73.6	142.3 ± 8.0	2.38 ± 0.139	24.33 ± 2.15	708.4 ± 36.8
	95.3	152.3 ± 10.1	2.54 ± 0.168	30.69 ± 2.66	784.0 ± 60.9
U-HPC	25.1	89.6 ± 6.5	1.49 ± 0.108	9.70 ± 1.72	148.2 ± 3.4
	46	106.9 ± 3.8	1.78 ± 0.063	14.60 ± 1.80	213.6 ± 20.5
	68	137.1 ± 7.1	2.28 ± 0.118	20.66 ± 1.51	510.3 ± 21.9
	106	148.5 ± 13.8	2.47 ± 0.212	30.37 ± 2.49	1017.3 ± 58.0
G1-HPC	28.0	100.3 ± 9.2	1.58 ± 0.145	10.02 ± 0.89	129.5 ± 11.1
	54.6	117.2 ± 4.6	1.84 ± 0.072	17.58 ± 2.07	478.4 ± 32.5
	73.2	147.6 ± 8.0	2.31 ± 0.125	21.27 ± 1.13	659.6 ± 44.6
	95.2	165.7 ± 12.9	2.61 ± 0.203	31.97 ± 2.93	1072.4 ± 95.4
G2-HPC	28.7	90.1 ± 10.5	1.45 ± 0.169	12.74 ± 1.17	231.8 ± 13.1
	56.4	144.8 ± 5.9	2.32 ± 0.095	17.48 ± 1.30	470.3 ± 19.3
	73.3	177.8 ± 11.1	2.85 ± 0.178	23.06 ± 1.48	709.8 ± 36.2
	105.9	198.3 ± 14.2	3.18 ± 0.228	32.37 ± 2.85	1209.4 ± 93.1

impact surfaces also contributed to the strength improvement under high strain rates [68].

Fig. 22 illustrates the effect of 3D re-entrant lattice reinforcement on dynamic compressive strength at similar strain rates. At a strain rate of around 28.1 s<sup>-1</sup>, the dynamic strength of P-HPC was 111.6 MPa, which was 11.3–24.6 % higher than that of lattice reinforced HPC. However, with the increase of strain rate from around 28.1 s<sup>-1</sup> to 72.0 s<sup>-1</sup>, lattice reinforced HPC exhibited a much higher enhancement of dynamic strength than P-HPC. Multiple macro-cracks were rapidly formed in P-

HPC, leading to the ultimate failure. In comparison, the augment confinement of 3D re-entrant lattices became stronger under high-speed impact. The unit cells of 3D re-entrant lattices contracted inward under dynamic compression to achieve a tri-axial compression state of concrete inside, which resisted the initiation and propagation of cracks [12]. Meanwhile, the re-entrant lattices converged towards the impact region and induced intense densification in impact area, enhancing the impact resistance and energy absorption capacity of the composites [8]. The augment reinforcement effects balanced the significant strength



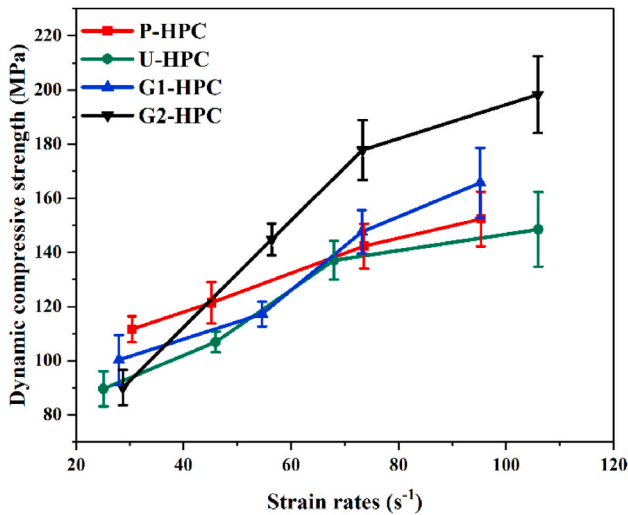


Fig. 22. Effect of 3D re-entrant lattice reinforcement on dynamic compressive strength of HPC at various strain rates.

difference between lattice and HPC with the increase of strain rate. Moreover, the strength of graded lattice reinforced HPC increased rapidly, surpassing both U-HPC and P-HPC (above around  $50.6 \text{ s}^{-1}$  in this study). G2-HPC had the highest dynamic compressive strength of 198.3 MPa at a strain rate of about  $100.6 \text{ s}^{-1}$ , followed by G1-HPC (165.7 MPa), P-HPC (152.3 MPa) and U-HPC (148.5 MPa). By introducing the heterogeneous structures to HPC, the spreading velocity, peak stress and peak strain energy could be reduced, while the impact time could be increased [80]. Meanwhile, the high-strength regions of graded lattice reinforced HPC specimens tended to provide a higher dynamic compressive resistance to delay the crack growth. G2-HPC had better dynamic compressive properties than G1-HPC. The impact resistance of the region reinforced by thicker re-entrant struts can be improved owing to the enhanced reinforcing effects of auxetic lattices [17]. The stress wave propagation path of G2-HPC was optimised as compared with G1-HPC. In the initial stage of G2-HPC under high strain rate, it could take three to four cycles for the stress wave to propagate within the specimen to reach a state of stress equilibrium [81]. During this process, the stress wave first encountered the regions with stronger strength and confinement, which effectively mitigated the impact energy, alleviated stress concentrations in subsequent relatively weaker regions, and consequently prevented premature failure [82]. The wave speed increased accordingly as the stress wave firstly propagated through the higher-strength region [83], leading to the more evenly distributed energy and the alleviation of stress concentration. The presence of graded layers delayed the concentration of wave energy, which could progressively transmit and disperse across the layers, thereby extending the formation process of the peak energy.

Fig. 23 shows the ultimate strain of all HPC specimens, indicating the deform capacity until final failure [84]. The ultimate strains were improved from around 1 %–3 % with the increasing strain rate for all specimens. The ultimate strain of lattice reinforced HPC was similar to that of P-HPC, suggesting that the PA12 based 3D re-entrant lattices had an insignificant effect on ductility of HPC under impact.

### 3.3.3. Dynamic increase factor (DIF)

Herein, dynamic increase factor (DIF) was adopted to evaluate the strain rate dependence of HPC specimens, which was defined as the ratio of the dynamic and corresponding quasi-static compressive strength [85]. Table 3 lists the results of DIF of all HPC specimens at various strain rates. All DIF values were higher than 1 at the strain rates ranging from  $28.1 \text{ s}^{-1}$  to  $100.6 \text{ s}^{-1}$ , implying that the dynamic compressive strength of plain HPC and lattice reinforced HPC was improved against

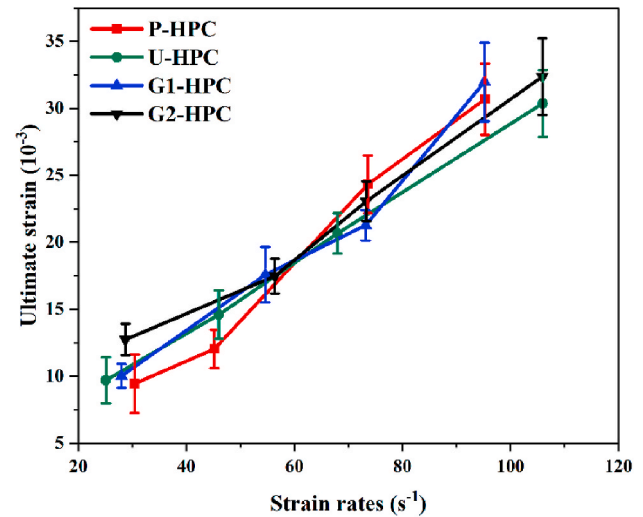


Fig. 23. Effect of 3D re-entrant lattice reinforcement on ultimate strain of HPC at various strain rates.

the static compressive strength, consistent with the findings on dynamic properties of high-strength concrete [86]. As mentioned above, the increase in dynamic compressive strength of HPC specimens can be ascribed to energy balance theory, inertia effect and lateral confinement. As seen in Fig. 24, all HPC specimens had a DIF of around 1.6 at a strain rate of around  $28.1 \text{ s}^{-1}$  and DIF increased with strain rates. Among all specimens, G2-HPC had the fastest rise in DIF. When the strain rate reached around  $100.6 \text{ s}^{-1}$ , DIF of G2-HPC was 25.2 %, 28.7 % and 22.3 % higher than that of P-HPC, U-HPC and G1-HPC, respectively, suggesting that the optimisation in geometrical configuration of re-entrant lattices can result in an improvement in reinforcement effect.

DIF of concrete was usually expressed as a semi-logarithmic function of strain rate [87,88]. As shown in Fig. 25, the linear fitted functions between DIF and logarithmic strain rate were derived. The fitted straight line of G2-HPC had a much higher slope, implying the great effect of suitable functionally gradient design of lattice on dynamic compressive strength of HPC at various strain rates. Table 4 summarises the linearly fitted DIF equations and correlation coefficients ( $R^2$ ) for different specimens.  $R^2$  values of the linear fitting curves were found to be 0.908–0.988, indicating a good fitting of the semi-logarithmic relationship between DIF and strain rate using experimental data [48].

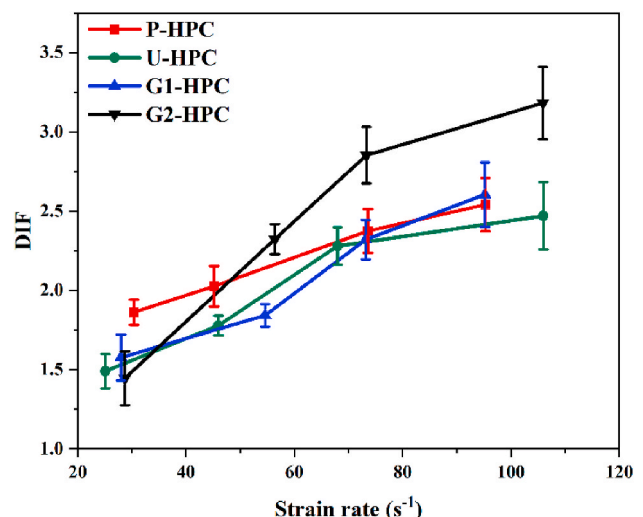


Fig. 24. Relationship between DIF and strain rate for all specimens.



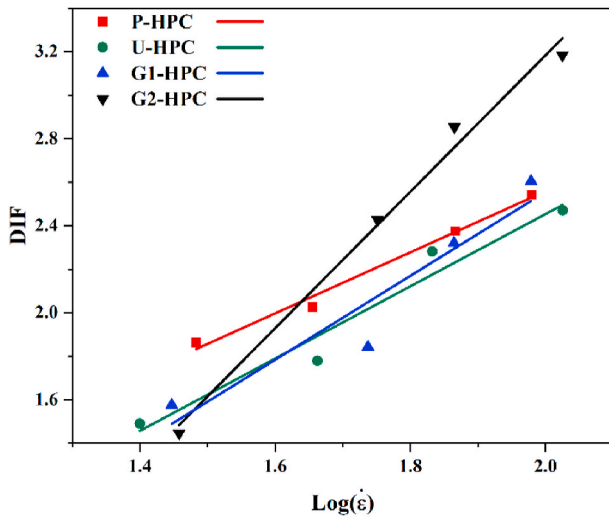


Fig. 25. Fitted linear curves of DIF against logarithm of strain rate.

Table 4

Summary of the linear fitting equations of DIF for different specimens.

Sample	Fitted equation of DIF	Correlation coefficient ( $R^2$ )
P-HPC	$DIF = 1.4032 \log \dot{\epsilon} - 0.2479$	0.988
U-HPC	$DIF = 1.6605 \log \dot{\epsilon} - 0.8673$	0.957
G1-HPC	$DIF = 1.9281 \log \dot{\epsilon} - 1.3010$	0.908
G2-HPC	$DIF = 3.1361 \log \dot{\epsilon} - 3.0884$	0.990

### 3.3.4. Dissipated energy

The energy absorption capacity of HPC specimens at various strain rates was commonly regarded as an indicator of toughness [75,89]. The energy difference between the incident wave, reflected wave and transmitted wave tended to be the energy dissipated by the deformation of the specimen. Hence, the fracture energy and total energy of HPC specimens under SHPB tests can be expressed as [90]:

$$W(t) = W_I(t) - W_R(t) - W_T(t) \quad (9)$$

where  $W(t)$  denotes the energy dissipated by the specimen, and  $W_I(t)$ ,  $W_R(t)$  and  $W_T(t)$  represent the energy of incident wave, reflected wave and transmitted waves, respectively.

Based on the elasticity of the bars, the elastic strain energy of incident, reflected and transmitted waves in the bars can be obtained as [91]:

$$W_n(t) = V \int_0^{\epsilon_n} \sigma d\epsilon = E_0 C_0 A_0 \int_0^t \epsilon_n^2(t) dt \quad (10)$$

where  $n = I, R, T$  denotes the incident wave, reflected wave and transmitted wave, respectively,  $V$  is the deformation volume of each bar, and  $E_0$ ,  $C_0$  and  $A_0$  represent the Young's modulus, elastic wave speed and cross-sectional area of the bars, respectively.

Fig. 26 presents the dissipated energy of HPC at various strain rates, indicating that the total energy of all HPC specimens was improved with the increase of strain rate. As the strain rate went up from around  $28.1 \text{ s}^{-1}$  to  $100.6 \text{ s}^{-1}$ , the dissipated energy of P-HPC, U-HPC, G1-HPC and G2-HPC was increased by 501.7 %, 586.4 %, 728.1 % and 421.7 %, respectively. The energy dissipation of normal concrete under impact mainly included the initiation of micro-cracks and macro-cracks and the propagation of cracks [48]. The increase of strain rates declined with the impact loading time, which reduced the propagation of cracks but promoted the formation of new cracks. Typically, the energy required to generate micro-cracks was greater than that for the existing cracks to propagate [68]. Hence, HPC specimens could dissipate more energy

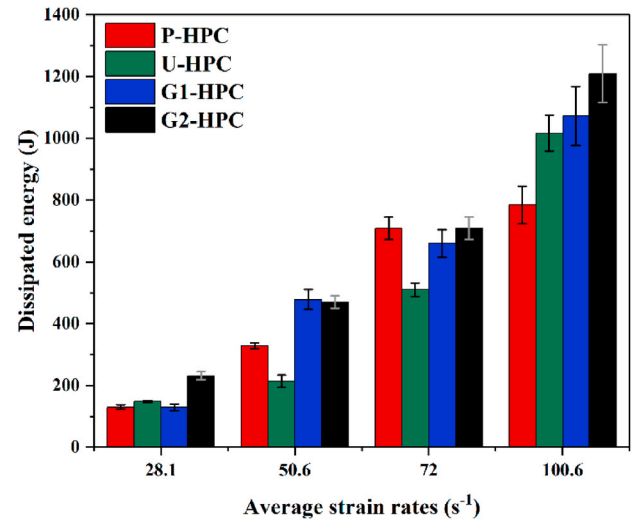


Fig. 26. Dynamic energy absorption capacity of HPC at various strain rates.

with the increasing strain rates. At low strain rates, lattice reinforced HPC had a similar energy absorption to P-HPC. However, when the strain rate reached around  $100.6 \text{ s}^{-1}$ , U-HPC, G1-HPC and G2-HPC had a respectively 29.8 %, 36.8 % and 54.3 % higher dissipated energy than P-HPC. As seen in Fig. 24, the strain before rapid decline region of P-HPC was much lower than that of lattice reinforced HPC specimens, implying that the brittleness of plain HPC can be improved through the incorporation of 3D re-entrant structures. The initiation and propagation of cracks can be delayed due to the tri-axial compression status of HPC at high strain rates [16]. The re-entrant structures could also converge towards the impact region, resulting in an enhanced impact resistance [8]. Moreover, the mutual constraints between HPC and lattice reinforcement also reduced the local deformation and the stress concentration of lattices [25], leading to a higher energy absorption through the bending and fracture of struts at high strain rates. The dissipated energy of G1-HPC and G2-HPC was  $-12.6\text{--}124.0\%$  and  $18.9\text{--}120.2\%$  respectively higher than that of U-HPC with the strain rates ranging from  $28.1 \text{ s}^{-1}$  to  $100.6 \text{ s}^{-1}$ . The graded latticed reinforced HPC had different elastic modulus and strength at different regions due to the gradient design of lattices. Hence, plastic deformation as well as formation and growth of micro-cracks could occur at different periods with the propagation of stress wave, which led to a more gradual and smooth dissipation of energy, and thereby improving the overall energy absorption capacity.

## 4. Conclusions

In this study, the static and dynamic behaviour of 3D re-entrant lattice reinforced high-performance concrete including uniform lattice reinforced HPC (U-HPC), positively graded lattice reinforced HPC (G1-HPC), negatively graded lattice reinforced HPC (G2-HPC) and plain HPC (P-HPC) was systematically investigated. Based on the obtained experimental results, the main conclusions can be drawn as follows:

- Static compressive strength of HPC specimens was slightly improved due to re-entrant lattice reinforcement. The lattice reinforced HPC exhibited superior energy absorption capacity, indicating a great potential for protective structures. The static compressive strength of P-HPC was 59.9 MPa, 0.3 %, 5.8 % and 3.9 % lower than U-HPC, G1-HPC and G2-HPC, respectively. The plastic dissipated energy of P-HPC was 346.5 J, which was 57.0 %, 54.6 % and 58.7 % lower than that of U-HPC, G1-HPC and G2-HPC, respectively.
- Compared to U structure, FG1 and FG2 had a relatively lower elastic modulus, yield stress and first peak stress, but 26.7 % and 19.2 %

higher energy absorption. U, FG1 and FG2 structures all exhibited significant NPR effects during static compressive process. FG1 and FG2 had more significant NPR effects in the layers with thinner struts.

- The incorporation of re-entrant lattice improved the dynamic compressive strength of HPC with the increase of strain rate from around  $28.1 \text{ s}^{-1}$  to  $72.0 \text{ s}^{-1}$ . G2-HPC had the highest dynamic compressive strength of 198.3 MPa at a strain rate of approximately  $100.6 \text{ s}^{-1}$ , followed by G1-HPC (165.7 MPa), P-HPC (152.3 MPa) and U-HPC (148.5 MPa).
- The total energy of all HPC specimens went up with the increase of strain rate. Although at low strain rates, lattice reinforced HPC had a similar energy absorption to P-HPC, U-HPC, G1-HPC and G2-HPC had a 29.8 %, 36.8 % and 54.3 % respectively higher dissipated energy than P-HPC when the strain rates reached around  $100.6 \text{ s}^{-1}$ . The gradient design of lattice reinforcement could lead to a more gradual and smooth dissipation of energy and thereby improving the overall energy absorption capacity.

The functionally graded 3D re-entrant lattice reinforced cementitious composites exhibit excellent mechanical performance under various impact scenarios and thus have broad potential applications. For future work, the effects of different factors including gradient magnitude, gradient direction, and strain rate conditions on compressive behaviour of 3D re-entrant lattice reinforced cementitious composites will be systematically investigated through an integrated experimental, theoretical and numerical programme to optimise and tailor the design of auxetic lattice reinforced cementitious composites with desirable performance for practical engineering applications. This is the subject of ongoing research and will be presented in future publications.

#### CRediT authorship contribution statement

**Yiwei Xuan:** Writing – original draft, Visualization, Validation, Methodology, Investigation, Formal analysis, Data curation. **Dianwei Gao:** Writing – review & editing, Resources, Methodology. **Mingzhong Zhang:** Writing – review & editing, Supervision, Project administration, Funding acquisition, Conceptualization.

#### Declaration of competing interest

The authors declare that they have no known competing financial interests or personal relationships that could have appeared to influence the work reported in this paper.

#### Acknowledgements

The authors gratefully acknowledge the financial support from the Royal Society (Award No. IEC\NSFC\233679) and University College London through a Global Engagement Grant. The financial support provided by National Natural Science Foundations of China (Grant No. 52201331) to D. Gao is also much appreciated.

#### Data availability

Data will be made available on request.

#### References

- [1] A. Neville, P.-C. Aitcin, High performance concrete—An overview, *Mater. Struct.* 31 (1998) 111–117.
- [2] C.S. Poon, Z. Shui, L. Lam, Compressive behavior of fiber reinforced high-performance concrete subjected to elevated temperatures, *Cement Concr. Res.* 34 (12) (2004) 2215–2222.
- [3] M. Chen, W. Chen, H. Zhong, D. Chi, Y. Wang, M. Zhang, Experimental study on dynamic compressive behaviour of recycled tyre polymer fibre reinforced concrete, *Cement Concr. Compos.* 98 (2019) 95–112.
- [4] O. Švec, G. Žirgulis, J.E. Bolander, H. Stang, Influence of formwork surface on the orientation of steel fibres within self-compacting concrete and on the mechanical properties of cast structural elements, *Cement Concr. Compos.* 50 (2014) 60–72.
- [5] M. Chen, H. Zhong, M. Zhang, Flexural fatigue behaviour of recycled tyre polymer fibre reinforced concrete, *Cement Concr. Compos.* 105 (2020) 103441.
- [6] B. Salazar, P. Aghdasi, I.D. Williams, C.P. Ostertag, H.K. Taylor, Polymer lattice-reinforcement for enhancing ductility of concrete, *Mater. Des.* 196 (2020) 109184.
- [7] R. Lakes, Foam structures with a negative Poisson's ratio, *Science* 235 (4792) (1987) 1038–1040.
- [8] N. Novak, L. Starčević, M. Vesenjak, Z. Ren, Blast response study of the sandwich composite panels with 3D chiral auxetic core, *Compos. Struct.* 210 (2019) 167–178.
- [9] H. Cho, D. Seo, D.-N. Kim, Mechanics of auxetic materials, in: S. Schmauder, C.-S. Chen, K.K. Chawla, N. Chawla, W. Chen, Y. Kagawa (Eds.), *Handbook of Mechanics of Materials*, Springer Singapore, Singapore, 2019, pp. 733–757.
- [10] Y. Yao, J.H. Park, L. Wang, X. Geng, J. Liu, P. Xu, H. Huang, S. Hollister, Y. Fan, Design, fabrication and mechanical properties of a 3D re-entrant metastructure, *Compos. Struct.* 314 (2023) 116963.
- [11] X. Xue, C. Lin, F. Wu, Z. Li, J. Liao, Lattice structures with negative Poisson's ratio: a review, *Mater. Today Commun.* 34 (2023) 105132.
- [12] G. Tzortzinis, A. Gross, S. Gerasimidis, Auxetic boosting of confinement in mortar by 3D reentrant truss lattices for next generation steel reinforced concrete members, *Extreme Mech. Lett.* 52 (2022) 101681.
- [13] G.G.C. Ngapeya, D. Waldmann, Overcome of bed-joint imperfections and improvement of actual contact in dry-stacked masonry, *Constr. Build. Mater.* 233 (2020) 117173.
- [14] T. Zahra, M. Dhanasekar, Characterisation and strategies for mitigation of the contact surface unevenness in dry-stack masonry, *Constr. Build. Mater.* 169 (2018) 612–628.
- [15] B.D. Scott, R. Park, M.J. Priestley, Stress-strain behavior of concrete confined by overlapping hoops at low and high strain rates, *J. Proceed.* (1982) 13–27.
- [16] M. Chen, Z. Chen, Y. Xuan, T. Zhang, M. Zhang, Static and dynamic compressive behaviour of 3D printed auxetic lattice reinforced ultra-high performance concrete, *Cement Concr. Compos.* 139 (2023) 105046.
- [17] H. Zhou, K. Jia, X. Wang, M.-X. Xiong, Y. Wang, Experimental and numerical investigation of low velocity impact response of foam concrete filled auxetic honeycombs, *Thin-Walled Struct.* 154 (2020) 106898.
- [18] R. Zhong, X. Ren, X.Y. Zhang, C. Luo, Y. Zhang, Y.M. Xie, Mechanical properties of concrete composites with auxetic single and layered honeycomb structures, *Constr. Build. Mater.* 322 (2022) 126453.
- [19] S.-P. Attard, *The Use of Auxetic Laminates as a Construction Material*, 2018.
- [20] C. Luo, X. Ren, D. Han, X.G. Zhang, R. Zhong, X.Y. Zhang, Y.M. Xie, A novel concrete-filled auxetic tube composite structure: design and compressive characteristic study, *Eng. Struct.* 268 (2022) 114759.
- [21] M. Asad, N. Win, T. Zahra, D.P. Thambiratnam, T.H. Chan, Y. Zhuge, Enhanced energy absorption of auxetic cementitious composites with polyurethane foam layers for building protection application, *J. Build. Eng.* 78 (2023) 107613.
- [22] M. Asad, M. Dhanasekar, T. Zahra, D. Thambiratnam, Impact Mitigation of Masonry Walls with Carbon Fibre and Auxetic Fibre Composite renders—A Numerical Study, *Structures*, Elsevier, 2020, pp. 2733–2751.
- [23] E.O. Momoh, A. Jayasinghe, M. Hajisadeghi, R. Vinai, K.E. Evans, P. Kripakaran, J. Orr, A state-of-the-art review on the application of auxetic materials in cementitious composites, *Thin-Walled Struct.* 196 (2024) 111447.
- [24] M. Chen, X. Yao, L. Zhu, M. Yin, Y. Xiong, N. Hu, Geometric design and performance of single and dual-printed lattice-reinforced cementitious composite, *Cement Concr. Compos.* 143 (2023) 105266.
- [25] T. Li, Y. Chen, X. Hu, Y. Li, L. Wang, Exploiting negative Poisson's ratio to design 3D-printed composites with enhanced mechanical properties, *Mater. Des.* 142 (2018) 247–258.
- [26] S.A. Tyagi, M. Manjaiah, Laser additive manufacturing of titanium-based functionally graded materials: a review, *J. Mater. Eng. Perform.* 31 (8) (2022) 6131–6148.
- [27] I. Maskery, A. Hussey, A. Panesar, A. Aremu, C. Tuck, I. Ashcroft, R. Hague, An investigation into reinforced and functionally graded lattice structures, *J. Cell. Plast.* 53 (2) (2017) 151–165.
- [28] S.R. Bates, I.R. Farrow, R.S. Trask, Compressive behaviour of 3D printed thermoplastic polyurethane honeycombs with graded densities, *Mater. Des.* 162 (2019) 130–142.
- [29] L. Yang, Y. Li, S. Wu, P. Chen, H. Wu, J. Su, H. Wang, J. Liu, C. Yan, Y. Shi, Tailorable and predictable mechanical responses of additive manufactured TPMS lattices with graded structures, *Mater. Sci. Eng., A* 843 (2022) 143109.
- [30] S.Y. Choy, C.-N. Sun, K.F. Leong, J. Wei, Compressive properties of Ti-6Al-4V lattice structures fabricated by selective laser melting: design, orientation and density, *Addit. Manuf.* 16 (2017) 213–224.
- [31] D.S. Al-Saedi, S. Masood, M. Faizan-Ur-Rab, A. Alomarrah, P. Ponnusamy, Mechanical properties and energy absorption capability of functionally graded F2BCC lattice fabricated by SLM, *Mater. Des.* 144 (2018) 32–44.
- [32] J.-H. Park, K. Park, Compressive behavior of soft lattice structures and their application to functional compliance control, *Addit. Manuf.* 33 (2020) 101148.
- [33] L. Bai, C. Gong, X. Chen, Y. Sun, L. Xin, H. Pu, Y. Peng, J. Luo, Mechanical properties and energy absorption capabilities of functionally graded lattice structures: experiments and simulations, *Int. J. Mech. Sci.* 182 (2020) 105735.
- [34] F. Günther, M. Wagner, S. Pilz, A. Gebert, M. Zimmermann, Design procedure for triply periodic minimal surface based biomimetic scaffolds, *J. Mech. Behav. Biomed. Mater.* 126 (2022) 104871.

- [35] H. Niknam, A. Akbarzadeh, Graded lattice structures: simultaneous enhancement in stiffness and energy absorption, *Mater. Des.* 196 (2020) 109129.
- [36] Y. Xiong, Z. Han, J. Qin, L. Dong, H. Zhang, Y. Wang, H. Chen, X. Li, Effects of porosity gradient pattern on mechanical performance of additive manufactured Ti-6Al-4V functionally graded porous structure, *Mater. Des.* 208 (2021) 109911.
- [37] F. Caiazzo, V. Alfieri, S.L. Campanelli, V. Errico, Additive manufacturing and mechanical testing of functionally-graded steel strut-based lattice structures, *J. Manuf. Process.* 83 (2022) 717–728.
- [38] I. Maskery, N. Aboulkhair, A. Aremu, C. Tuck, I. Ashcroft, R.D. Wildman, R. Hague, A mechanical property evaluation of graded density Al-Si10-Mg lattice structures manufactured by selective laser melting, *Mater. Sci. Eng., A* 670 (2016) 264–274.
- [39] S. Yu, J. Sun, J. Bai, Investigation of functionally graded TPMS structures fabricated by additive manufacturing, *Mater. Des.* 182 (2019) 108021.
- [40] X.-T. Wang, Y.-L. Chen, L. Ma, The manufacture and characterization of composite three-dimensional re-entrant auxetic cellular structures made from carbon fiber reinforced polymer, *J. Compos. Mater.* 52 (23) (2018) 3265–3273.
- [41] W. Griebel, D. Ruestem, Nylon-12-preparation, properties, and applications, *Ind. Eng. Chem.* 62 (3) (1970) 16–22.
- [42] M. Zhao, D. Drummer, K. Wudy, M. Drexler, Sintering study of polyamide 12 particles for selective laser melting, *Int. J. Recent Contributions from Eng. Sci. IT (iJES)* 3 (1) (2015) 28–33.
- [43] L. Zárybnická, J. Petrů, P. Krpec, M. Pagáč, Effect of additives and print orientation on the properties of laser sintering-printed polyamide 12 components, *Polymers* 14 (6) (2022) 1172.
- [44] S.A.f.M. Regulation, S.A.o.t.P.s.R.o. China, *Plastics – Determination of Tensile Properties, Part 2: Test Conditions for Moulding and Extrusion Plastics*, 2022. China.
- [45] M.o.H.a.U.-R. Development, *Standard for Test Method of Basic Properties of Construction Mortar*, China Architecture Publishing & Media Co Ltd, China, 2009.
- [46] S. Nemat-Nasser, Introduction to high strain rate testing, *ASM handbook 8* (2000) 427–428.
- [47] R. Naghdabadi, M.J. Ashrafi, J. Arghavani, Experimental and numerical investigation of pulse-shaped split hopkinson pressure bar test, *Mater. Sci. Eng., A* 539 (2012) 285–293.
- [48] H. Zhang, L. Wang, K. Zheng, T.J. Bakura, P.G. Totakhal, Research on compressive impact dynamic behavior and constitutive model of polypropylene fiber reinforced concrete, *Constr. Build. Mater.* 187 (2018) 584–595.
- [49] J. Xiao, L. Li, L. Shen, C.S. Poon, Compressive behaviour of recycled aggregate concrete under impact loading, *Cement Concr. Res.* 71 (2015) 46–55.
- [50] Y. Yang, Q. Li, L. Qiao, Review of SHPB dynamic load impact test characteristics and energy analysis methods, *Processes* 11 (10) (2023) 3029.
- [51] P. Bischoff, S. Perry, Compressive behaviour of concrete at high strain rates, *Mater. Struct.* 24 (1991) 425–450.
- [52] S.P. Timoshenko, J.M. Gere, *Theory of Elastic Stability*, 2012. Courier Corporation.
- [53] L. Yang, O. Harrysson, H. West, D. Cormier, Compressive properties of Ti-6Al-4V auxetic mesh structures made by electron beam melting, *Acta Mater.* 60 (8) (2012) 3370–3379.
- [54] H.H. Xu, H.C. Luo, X.G. Zhang, W. Jiang, X.C. Teng, W.Q. Chen, J. Yang, Y.M. Xie, X. Ren, Mechanical properties of aluminum foam filled re-entrant honeycomb with uniform and gradient designs, *Int. J. Mech. Sci.* 244 (2023) 108075.
- [55] L. Yang, O. Harrysson, H. West, D. Cormier, Modeling of uniaxial compression in a 3D periodic re-entrant lattice structure, *J. Mater. Sci.* 48 (4) (2013) 1413–1422.
- [56] Y. Xue, X. Wang, W. Wang, X. Zhong, F. Han, Compressive property of Al-based auxetic lattice structures fabricated by 3-D printing combined with investment casting, *Mater. Sci. Eng., A* 722 (2018) 255–262.
- [57] Y. Lin, W. Shi, J. Li, Y. Liu, S. Liu, J. Li, Evaluation of mechanical properties of Ti-6Al-4V BCC lattice structure with different density gradient variations prepared by L-PBF, *Mater. Sci. Eng., A* 872 (2023) 144986.
- [58] Q. Li, I. Magkiriadis, J.J. Harrigan, Compressive strain at the onset of densification of cellular solids, *J. Cell. Plast.* 42 (5) (2006) 371–392.
- [59] C. Rodrigo, S. Xu, Y. Durand, D. Fraser, R. Ruan, Quasi-static and dynamic compression of additively manufactured functionally graded lattices: experiments and simulations, *Eng. Struct.* 284 (2023) 115909.
- [60] Y. Lin, W. Shi, X. Sun, S. Liu, J. Li, Y. Zhou, Y. Han, Influence of density gradient on the compression of functionally graded BCC lattice structure, *Materials* 16 (2) (2023) 520.
- [61] S.R. de Galarreta, R.J. Doyle, J. Jeffers, S. Ghouse, Laser powder bed fusion of porous graded structures: a comparison between computational and experimental analysis, *J. Mech. Behav. Biomed. Mater.* 123 (2021) 104784.
- [62] T. Zhang, M. Zhang, Y. Shen, H. Zhu, Z. Yan, Mitigating the damage of ultra-high performance concrete at elevated temperatures using synergistic flame-retardant polymer fibres, *Cement Concr. Res.* 158 (2022) 106835.
- [63] T. Li, Y. Chen, L. Wang, Enhanced fracture toughness in architected interpenetrating phase composites by 3D printing, *Compos. Sci. Technol.* 167 (2018) 251–259.
- [64] W. Zhou, R.J. Bol, Y. Zhou, Z. Meng, Y. Xu, J. Xie, B. Šavija, Reinforcing mechanism of lattice-reinforced cementitious composites: insight into flexural performance and material interactions, *Mater. Des.* (2025) 114332.
- [65] T. Li, F. Liu, L. Wang, Enhancing indentation and impact resistance in auxetic composite materials, *Compos. B Eng.* 198 (2020) 108229.
- [66] M.F.A. Lorna Gibson, *Cellular Solids: Structure and Properties*, second ed., Cambridge University Press, Cambridge, 1997.
- [67] T.-S. Eom, H.-G. Park, Evaluation of energy dissipation of slender reinforced concrete members and its applications, *Eng. Struct.* 32 (9) (2010) 2884–2893.
- [68] Y. Wang, Z. Wang, X. Liang, M. An, Experimental and numerical studies on dynamic compressive behavior of reactive powder concretes, *Acta Mech. Solida Sin.* 21 (5) (2008) 420–430.
- [69] W.W. Chen, B. Song, Split Hopkinson (Kolsky) Bar: Design, Testing and Applications, Springer Science & Business, 2010. Media.
- [70] S. Jiang, L. Shen, W. Li, An experimental study of aggregate shape effect on dynamic compressive behaviours of cementitious mortar, *Constr. Build. Mater.* 303 (2021) 124443.
- [71] X. Hou, S. Cao, W. Zheng, Q. Rong, G. Li, Experimental study on dynamic compressive properties of fiber-reinforced reactive powder concrete at high strain rates, *Eng. Struct.* 169 (2018) 119–130.
- [72] L. Yang, O. Harrysson, H. West, D. Cormier, Mechanical properties of 3D re-entrant honeycomb auxetic structures realized via additive manufacturing, *Int. J. Solid Struct.* 69 (2015) 475–490.
- [73] Z. Wu, C. Shi, W. He, D. Wang, Static and dynamic compressive properties of ultra-high performance concrete (UHPC) with hybrid steel fiber reinforcements, *Cement Concr. Compos.* 79 (2017) 148–157.
- [74] Y. Lu, K. Xu, Modelling of dynamic behaviour of concrete materials under blast loading, *Int. J. Solid Struct.* 41 (1) (2004) 131–143.
- [75] X. Guan, X. Hou, X. Hao, Y. Liu, F. Li, P. Hou, Dynamic energy performance and pore structure of CGSC under sulfate attack: an SHPB-based study, *Constr. Build. Mater.* 457 (2024) 139457.
- [76] Q. Li, H. Meng, About the dynamic strength enhancement of concrete-like materials in a split Hopkinson pressure bar test, *Int. J. Solid Struct.* 40 (2) (2003) 343–360.
- [77] D. Cotsovos, M. Pavlović, Numerical investigation of concrete subjected to compressive impact loading. Part 1: a fundamental explanation for the apparent strength gain at high loading rates, *Comput. Struct.* 86 (1–2) (2008) 145–163.
- [78] D. Cotsovos, M. Pavlović, Numerical investigation of concrete subjected to compressive impact loading. Part 2: parametric investigation of factors affecting behaviour at high loading rates, *Comput. Struct.* 86 (1–2) (2008) 164–180.
- [79] L. Jie, A review on the constitutive model for static and dynamic damage of concrete, *力学进展* 40 (3) (2010) 284–298.
- [80] C. Zhao, M. Zhang, G. Li, D. Wang, Stress wave propagation and energy absorption properties of heterogeneous lattice materials under impact load, *Adv. Mater. Sci. Eng.* 2021 (1) (2021) 1766952.
- [81] K. Xia, W. Yao, Dynamic rock tests using split Hopkinson (Kolsky) bar system—A review, *J. Rock Mech. Geotech. Eng.* 7 (1) (2015) 27–59.
- [82] D. Hui, P.K. Dutta, A new concept of shock mitigation by impedance-graded materials, *Compos. B Eng.* 42 (8) (2011) 2181–2184.
- [83] T. Yu, P. Xue, *Introduction to Engineering Plasticity: Fundamentals with Applications in Metal Forming, Limit Analysis and Energy Absorption*, 2022. Elsevier.
- [84] F. Liu, G. Chen, L. Li, Y. Guo, Study of impact performance of rubber reinforced concrete, *Constr. Build. Mater.* 36 (2012) 604–616.
- [85] H. Fan, H. Yu, H. Ma, Dynamic increase factor (DIF) of concrete with SHPB tests: review and systematic analysis, *J. Build. Eng.* (2023) 107666.
- [86] Y. Guo, G. Gao, L. Jing, V. Shim, Response of high-strength concrete to dynamic compressive loading, *Int. J. Impact Eng.* 108 (2017) 114–135.
- [87] L. Jin, J. Li, W. Yu, X. Du, Size effect modelling for dynamic biaxial compressive strength of concrete: influence of lateral stress ratio and strain rate, *Int. J. Impact Eng.* 156 (2021) 103942.
- [88] G. Ren, H. Wu, Q. Fang, J. Liu, Effects of steel fiber content and type on dynamic compressive mechanical properties of UHPCC, *Constr. Build. Mater.* 164 (2018) 29–43.
- [89] L. Jin, R. Zhang, Y. Tian, G. Dou, X. Du, Experimental investigation on static and dynamic mechanical properties of steel fiber reinforced ultra-high-strength concretes, *Constr. Build. Mater.* 178 (2018) 102–111.
- [90] B. Song, W. Chen, Energy for specimen deformation in a split Hopkinson pressure bar experiment, *Exp. Mech.* 46 (2006) 407–410.
- [91] W. Feng, F. Liu, F. Yang, L. Li, L. Jing, Experimental study on dynamic split tensile properties of rubber concrete, *Constr. Build. Mater.* 165 (2018) 675–687.